

1 **Integrating faults and past earthquakes into a probabilistic seismic hazard**  
2 **model for peninsular Italy**

3  
4 Alessandro Valentini<sup>1</sup>, Francesco Visini<sup>2</sup> and Bruno Pace<sup>1</sup>

5 <sup>1</sup> DiSPUTer, Università degli Studi “Gabriele d’Annunzio”, Chieti, Italy

6 <sup>2</sup> Istituto Nazionale di Geofisica e Vulcanologia, L’Aquila, Italy

7  
8 **Abstract**

9  
10 *Italy is one of the most seismically active countries in Europe. Moderate to strong earthquakes, with magnitudes of up to ~7, have been historically recorded for many active faults. Currently, probabilistic seismic hazard assessments in Italy are mainly based on area source models, in which seismicity is modelled using a number of seismotectonic zones and the occurrence of earthquakes is assumed uniform. However, in the past decade, efforts have increasingly been directed towards using fault sources in seismic hazard models to obtain more detailed and potentially more realistic patterns of ground motion. In our model, we used two categories of earthquake sources. The first involves active faults, and fault slip rates were used to quantify the seismic activity rate. We produced an inventory of all fault sources with details of their geometric, kinematic and energetic properties. The associated parameters were used to compute the total seismic moment rate of each fault. We evaluated the magnitude-frequency distribution (MFD) of each fault source using two models: a characteristic Gaussian model centred on the maximum magnitude and a Truncated Gutenberg-Richter model. The second earthquake source category involves distributed seismicity, and a fixed-radius smoothed approach and a historical catalogue were used to evaluate seismic activity. Under the assumption that deformation is concentrated along faults, we combined the MFD derived from the geometry and slip rates of active faults with the MFD from the spatially smoothed earthquake sources and assumed that the smoothed seismic activity in the vicinity of an active fault gradually decreases by a fault size-driven factor. Additionally, we computed horizontal peak ground acceleration maps for return periods of 475 and 2,475 yrs. Although the ranges and gross spatial distributions of the expected accelerations obtained here are comparable to those obtained through methods involving seismic catalogues and classical zonation models, the spatial pattern of the hazard maps obtained with our model is far more detailed. Our model is characterized by areas that are more hazardous and that correspond to mapped active faults, while previous models yield expected accelerations that are almost uniformly distributed across large regions. In addition, we conducted sensitivity tests to*

34 *determine the impact on the hazard results of the earthquake rates derived from two MFD models for*  
35 *faults and to determine the relative contributions of faults versus distributed seismic activity. We*  
36 *believe that our model represents advancements in terms of the input data (quantity and quality) and*  
37 *methodology used in the field of fault-based regional seismic hazard modelling in Italy.*

38

## 39 **1. Introduction**

40 In this paper, we present the results of a new probabilistic seismic hazard (PSH)  
41 model for Italy that includes significant advances in the use of integrated active fault  
42 and seismological data. The use of active faults as an input for PSH analysis is a  
43 consolidated approach in many countries characterized by high strain rates and  
44 seismic releases, as shown, for example, by Field et al. (2015) in California and  
45 Stirling et al. (2012) in New Zealand. However, in recent years, active fault data have  
46 also been successfully integrated into PSH assessments in regions with moderate-  
47 to-low strain rates, such as SE Spain (e.g., Garcia-Mayordomo et al., 2007), France  
48 (e.g., Scotti et al., 2014), and central Italy (e.g., Peruzza et al., 2011).

49 In Europe, a working group of the European Seismological Commission, named  
50 *Fault2SHA*, is discussing fault-based seismic hazard modelling  
51 (<https://sites.google.com/site/linkingfaultpsha/home>). The working group, born to  
52 motivate exchanges between field geologists, fault modellers and seismic hazard  
53 practitioners, organizes workshops, conference sessions, and special issues and  
54 stimulates collaborations between researchers. The work we are presenting here  
55 stems from the activities of the *Fault2SHA* working group.

56 Combining active faults and background sources is one of the main issues in this  
57 type of approach. Although the methodology remains far from identifying a standard  
58 procedure, common approaches combine active faults and background sources by  
59 applying a threshold magnitude, generally between 5.5 and 7, above which  
60 seismicity is modelled as occurring on faults and below which seismicity is modelled  
61 via a smoothed approach (e.g., Akinci et al., 2009), area sources (e.g., the so-called  
62 FSBG model in SHARE; Woessner et al., 2015) or a combination of the two (Field et  
63 al., 2015; Pace et al., 2006).

64 Another important issue in the use of active faults in PSHA is assigning the “correct”  
65 magnitude-frequency distribution (MFD) to the fault sources. Gutenberg-Richter (GR)



66 and characteristic earthquake models are commonly used, and the choice  
67 sometimes depends on the knowledge of the fault and data availability. Often, the  
68 choice of the “appropriate” MFD for each fault source is a difficult task because  
69 palaeoseismological studies are scarce, and it is often difficult to establish clear  
70 relationships between mapped faults and historical seismicity. Recently, Field et al.  
71 (2017) discussed the effects and complexity of the choice, highlighting how often the  
72 GR model results are not consistent with data; however, in other cases,  
73 uncharacteristic behaviour, with rates smaller than the maximum, are possible. The  
74 discussion is open (see for example the discussion by Kagan et al., 2012) and far  
75 from being solved with the available observations, including both seismological  
76 and/or geological/paleoseismological observations. In this work, we explore the  
77 calculations of these two MFDs, a characteristic Gaussian model and a Truncated  
78 Gutenberg-Richter model, to explore the epistemic uncertainties and to consider a  
79 *Mixed model* as a so-called “expert judgement” model. This approach is useful for  
80 comparative analysis, and which we assigned one of the two MFDs to each fault  
81 source. The rationale of the choice of the MFD of each fault source is explained in  
82 detail later in this paper. However, this approach obviously does not solve the issue,  
83 and the choice of MFD remains an open question in fault-based PSHA.

84 In Italy, the current national PSH model for building code (Stucchi et al., 2011) is  
85 based on area sources and the classical Cornell approach (Cornell, 1968), in which  
86 the occurrence of earthquakes is assumed uniform in the defined seismotectonic  
87 zones. However, we believe that more efforts must be directed towards using  
88 geological data (e.g., fault sources and paleoseismological information) in PSH  
89 models to obtain detailed patterns of ground motion, extend the observational time  
90 required to capture the recurrence of large-magnitude events and improve the  
91 reliability of seismic hazard assessments. In fact, as highlighted by the 2016-2017  
92 seismic sequences in central Italy, a zone-based PSH is not able to model local  
93 spatial variations in ground motion (Meletti et al., 2016), whereas a fault-based  
94 model can provide insights for aftershock time-dependent PSH analysis (Peruzza et  
95 al., 2016). In conclusion, even if the main purpose of this work is to integrate active  
96 faults into hazard calculations for the Italian territory, this study does not represent  
97 an official update of the seismic hazard model of Italy.

98

99 **2. Source Inputs**

100 Two earthquake-source inputs are considered in this work. The first is a fault source  
101 input that is based on active faults and uses the geometries and slip rates of known  
102 active faults to compute activity rates over a certain range of magnitude.<sup>S</sup>The second  
103 is a classical smoothed approach that accounts for the rates of expected  
104 earthquakes with a minimum moment magnitude (Mw) of 4.5 but excludes  
105 earthquakes associated with known faults based on a modified earthquake  
106 catalogue. Note that our PSH model requires the combination of the two source  
107 inputs related to the locations of expected seismicity rates into a single model.  
108 Therefore, these two earthquake-source inputs are not independent but  
109 complementary, in both the magnitude and frequency distribution, and together  
110 account for all seismicity in Italy.

111 In the following subsections, we describe the two source inputs and how they are  
112 combined in the PSH model.

113 **2.1 Fault Source Input**

114 In seismic hazard assessment, an active fault is a structure that exhibits evidence of  
115 activity in the late Quaternary (i.e., in the past 125 kyr), has a demonstrable or  
116 potential capability of generating major earthquakes and is capable of future  
117 reactivation (see Machette, 2000 for a discussion on terminology). The evidence of  
118 Quaternary activity can be geomorphological and/or paleoseismological when  
119 activation information from instrumental seismic sequences and/or association to  
120 historical earthquakes is not available. Fault source inputs are useful for seismic  
121 hazard studies, and we compiled a database for Italy via the analysis and synthesis  
122 of neotectonic and seismotectonic data from approximately 90 published studies of  
123 110 faults across Italy. Our database included, but was not limited to, the Database  
124 of Individual Seismogenic Sources (DISS vers. 3.2.0, <http://diss.rm.ingv.it/diss/>),  
125 which is already available for Italy. It is important to highlight that the DISS is  
126 currently composed of two main categories of seismogenic sources: individual and  
127 composite sources. The latter are defined by the DISS' authors as “*simplified and*  
128 *three-dimensional representation of a crustal fault containing an unspecified number*  
129 *of seismogenic sources that cannot be singled out. Composite seismogenic sources*  
130 *are not associated with a specific set of earthquakes or earthquake distribution*”, and

131 therefore are not useful for our PSHA approach; the former is “*a simplified and three-*  
132 *dimensional representation of a rectangular fault plane. Individual seismogenic*  
133 *sources are assumed to exhibit characteristic behaviour with respect to rupture*  
134 *length/width and expected magnitude*” (<http://diss.rm.ingv.it/diss/index.php/about/13-introduction>). Even if in agreement with our approach, we note that some of the  
136 individual seismogenic sources in the DISS are based on geological and  
137 paleoseismological information, and many others used the *Boxer* code (Gasperini et  
138 al., 1999) to calculate the epicentre, moment magnitude, size and orientation of a  
139 seismic source from observed macroseismic intensities. We carefully analysed the  
140 individual sources and some related issues: (i) the lack of updating of the geological  
141 information of some individual sources and (ii) the nonconformity between the input  
142 data used by DISS in *Boxer* and the latest historical seismicity (CPTI15) and  
143 macroseismic intensity (DBMI15) publications. Thus, we performed a full review of  
144 the fault database. We then compiled a fault source database as a synthesis of  
145 works published over the past twenty years, including DISS, using all updated and  
146 available geological, paleoseismological and seismological data (see the  
147 supplemental files for a complete list of references). We consider our database as  
148 complete as possible in terms of individual seismogenic sources, and it contains all  
149 the parameters necessary to construct an input dataset for fault-based PSHA.

150 The resulting database of normal and strike-slip active and seismogenic faults in  
151 peninsular Italy (Fig. 1, Tables 1 and 2; see the supplemental files) includes all the  
152 available geometric, kinematic, slip rate and earthquake source-related information.  
153 In the case of missing data regarding the geometric parameters of dip and rake, we  
154 assumed typical dip and rake values of 60° and -90°, respectively, for normal faults  
155 and 90° and 0° or 180°, respectively, for strike-slip faults. In this paper, only normal  
156 and strike-slip faults are used as fault source inputs. We decided not to include thrust  
157 faults in the present study because, with the methodology proposed in this study (as  
158 discussed later in the text), the maximum size of a single-rupture segment must be  
159 defined, and segmentation criteria have not been established for large thrust zones.  
160 Moreover, our method uses slip rates to derive active seismicity rates, and sufficient  
161 knowledge of these values is not available for thrust faults in Italy. Because some  
162 areas of Italy, such as the NW sector of the Alps, Po Valley, the offshore sector of  
163 the central Adriatic Sea, and SW Sicily, may be excluded by this limitation, we are

164 considering an update to our approach to include thrust faults and volcanic sources  
165 in a future study. The upper and lower boundaries of the seismogenic layer are  
166 mainly derived from the analysis of Stucchi et al. (2011) of the Italian national  
167 seismic hazard model and locally refined by more detailed studies (Boncio et al.,  
168 2011; Peruzza et al., 2011; Ferranti et al., 2014).

169 Based on the compiled database, we explored three main issues associated with  
170 defining a fault source input: the slip rate evaluation, the segmentation model and  
171 the expected seismicity rate calculation.

172 *2.1.1 Slip rates*

173 Slip rates control fault-based seismic hazards (Main, 1996, Roberts et al., 2004; Bull  
174 et al., 2006; Visini and Pace, 2014) and reflect the velocities of the mechanisms that  
175 operate during continental deformation (e.g., Cowie et al., 2005). Moreover, long-  
176 term observations of faults in various tectonic contexts have shown that slip rates  
177 vary in space and time (e.g., Bull et al., 2006; Nicol et al., 2006, 2010, McClymont et  
178 al., 2009; Gunderson et al., 2013; Benedetti et al., 2013, D'Amato et al., 2016), and  
179 numerical simulations (e.g., Robinson et al., 2009; Cowie et al., 2012; Visini and  
180 Pace, 2014) suggest that variability mainly occurs in response to interactions  
181 between adjacent faults. Therefore, understanding the temporal variability in fault slip  
182 rates is a key point in understanding the earthquake recurrence rates and their  
183 variability.

184 In this work, we used the mean of the minimum and maximum slip rate values listed  
185 in Table 1 and assumed that it is representative of the long-term behaviour (over the  
186 past 15 ky in the Apennines). These values were derived from approximately 65  
187 available neotectonics, palaeoseismology and seismotectonics papers (see the  
188 supplemental files). To evaluate the long-term slip rate, which is representative of the  
189 average slip behaviour, and its variability over time, we used slip rates determined in  
190 different ways and at different time scales (e.g., at the decadal scale based on  
191 geodetic data or at longer scales based on the displacement of Holocene or Plio-  
192 Pleistocene horizons). Because a direct comparison of slip rates over different time  
193 intervals obtained by different methods may be misleading (Nicol et al., 2009), we  
194 cannot exclude the possibility that epistemic uncertainties could affect the original

195 data in some cases. The discussion of these possible biases and their evaluation via  
196 statistically derived approaches (e.g., Gardner et al., 1987; Finnegan et al., 2014;  
197 Gallen et al., 2015) is beyond the scope of this paper and will be explored in future  
198 work. Moreover, we are assuming that slip rate values used are representative of  
199 seismic movements, and aseismic factors are not taken into account. Therefore, we  
200 believe that investigating the effect of this assumption could be another issue  
201 explored in future work; for example, by differentiating between aseismic slip factors  
202 in different tectonic contexts.

203 Because 28 faults had no measured slip (or throw) rate (Fig. 1a), we proposed a  
204 statistically derived approach to assign a slip rate to these faults. Based on the slip  
205 rate spatial distribution shown in Figure 1b, we subdivided the fault database into  
206 three large regions—the Northern Apennines, Central-Southern Apennines and  
207 Calabria-Sicilian coast—and analysed the slip rate distribution in these three areas. In  
208 Figure 1b, the slip rates tend to increase from north to south. The fault slip rates in  
209 the Northern Apennines range from 0.3 to 0.8 mm/yr, with the most common ranging  
210 from approximately 0.5-0.6 mm/yr; the slip rates in the Central-Southern Apennines  
211 range from 0.3 to 1.0, and the most common rate is approximately 0.3 mm/yr; and  
212 the slip rates in the southern area (Calabria and Sicily) range from 0.9 to 1.8, with  
213 the most common being approximately 0.9 mm/yr.

214 The first step in assigning an average slip rate and a range of variability to the faults  
215 with unknown values is to identify the most representative distribution among known  
216 probability density functions using the slip rate data from each of the three areas. We  
217 test five well-known probability density functions (*Weibull*, *normal*, *exponential*,  
218 *Inverse Gaussian* and *gamma*) against mean slip rate observations. The resulting  
219 function with the highest log-likelihood is the *normal* function in all three areas. Thus,  
220 the mean value of the *normal* distribution is assigned to the faults with unknown  
221 values. We assign a value of 0.58 mm/yr to faults in the northern area, 0.64 mm/yr to  
222 faults in the Central-Southern area, and 1.10 mm/yr to faults in the Calabria-Sicilian  
223 area. To assign a range of slip rate variability to each of the three areas, we test the  
224 same probability density functions against slip rate variability observations. Similar to  
225 the mean slip rate, the probability density function with the highest log-likelihood is  
226 the *normal* function in all three areas. We assign a value of 0.25 mm/yr to the faults



227 in the northern area, 0.29 mm/yr to the faults in the Central-Southern area, and 0.35  
228 mm/yr to the faults in the Calabria-Sicilian area.

229

230 *2.1.2 Segmentation rules for delineating fault sources*

231 An important issue in the definition of a fault source input is the formulation of  
232 segmentation rules. In fact, the question of whether structural segment boundaries  
233 along multisegment active faults act as persistent barriers to a single rupture is  
234 critical to defining the maximum seismogenic potential of fault sources. In our case,  
235 the rationale behind the definition of a fault source is based on the assumption that  
236 the geometric and kinematic features of a fault source are expressions of its  
237 seismogenic potential and that its dimensions are compatible for hosting major (Mw  
238  $\geq 5.5$ ) earthquakes. Therefore, a fault source ~~is considered~~ a fault or an ensemble of  
239 faults that slip together during an individual major earthquake. A fault source is  
240 defined by a *seismogenic master fault* and its surface projection (Fig. 2a).  
241 *Seismogenic master faults* are separated from each other by first-order structural or  
242 geometrical complexities. Following the suggestions by Boncio et al. (2004) and  
243 Field et al. (2015), we imposed the following segmentation rules in our case study: (i)  
244 4-km fault gaps among aligned structures; (ii) intersections with cross structures  
245 (often transfer faults) extending 4 km along strike and oriented at nearly right angles  
246 to the intersecting faults; (iii) overlapping or underlapping en echelon arrangements  
247 with separations between faults of 4 km; (iv) bending  $\geq 60^\circ$  for more than 4 km; (v)  
248 average slip rate variability along a strike greater than or equal to 50%; and (vi)  
249 changes in seismogenic thickness greater than 5 km among aligned structures.  
250 Example applications of the above rules are illustrated in Figure 2a.

251 By applying the above rules to our fault database, the 110 faults yielded 86 fault  
252 sources: 9 strike-slip sources and 77 normal-slip sources. The longest fault source is  
253 *Castelluccio dei Sauri* (fault number (*id* in Table 1) 42, L = 93.2 km), and the shortest  
254 is *Castrovillari* (*id* 63, L = 10.3 km). The mean length is 30 km. The dip angle varies  
255 from  $30^\circ$  to  $90^\circ$ , and 70% of the fault sources have dip angles between  $50^\circ$  and  $60^\circ$ .  
256 The mean value of seismogenic thickness (ST) is approximately 12 km. The source  
257 with the largest ST is *Mattinata* (*id* 41, ST = 25 km), and the source with the thinnest

258 ST is *Monte Santa Maria Tiberina* (id 9, ST = 2.5 km) due to the presence of an east-  
259 dipping low angle normal fault, the Alto-Tiberina Fault (Boncio et al., 2000), located a  
260 few kilometres west of the Monte Santa Maria Tiberina fault. **Observed values of**  
261 **maximum magnitude** ( $M_w$ ) have been assigned to 35 fault sources (based on Table  
262 2), and the values vary from 5.90 to 7.32. The fault source inputs are shown in  
263 Figure 3.

264

### 265 2.1.3 Expected seismicity rates

266 Each fault source is characterized by data, such as kinematic, geometry and slip rate  
267 information, that we use as inputs for the FiSH code (Pace et al., 2016) to calculate  
268 the global budget of the seismic moment rate allowed by the structure. This  
269 calculation is based on predefined size-magnitude relationships in terms of the  
270 maximum magnitude ( $M_{max}$ ) and the associated mean recurrence time ( $T_{mean}$ ). Table  
271 1 summarizes the geometric parameters used as FiSH input parameters for each  
272 fault source (seismogenic box) shown in Figure 3. To evaluate  $M_{max}$  of each source,  
273 according to Pace et al., (2016) we first computed and then combined up to five  $M_{max}$   
274 **values** (see the example of the Paganica fault source in Fig. 2b, details in Pace et  
275 al., 2016). Specifically, these five  $M_{max}$  **values** are as follows:  $M_{M0}$  based on the  
276 calculated scalar seismic moment ( $M_0$ ) and the application of the standard formula  
277  $M_w = 2/3 (\log M_0 - 9.1)$  (Hanks and Kanamori, 1979; IASPEI, 2005); two magnitude  
278 **values** using the Wells and Coppersmith (1994) empirical relationships for the  
279 maximum subsurface rupture length (MRLD) and maximum rupture area (MRA); a  
280 **value** that corresponds to the maximum observed magnitude (MObs), if available;  
281 and a **value** (MASP, ASP for aspect ratio) computed by reducing the fault length  
282 **input** if the aspect ratio (W/L) is smaller than the value evaluated by the relation  
283 between the aspect ratio and rupture length of observed earthquake ruptures, as  
284 derived by Peruzza and Pace (2002) (not in the case of Paganica in Fig. 2b).  
285 Although **incorrect** to consider MObs a possible  $M_{max}$  value and treat it the same as  
286 other estimations, in some cases, it was useful to constrain the seismogenic  
287 potentials of individual seismogenic sources. As an example, for the *Irpinia Fault* (id  
288 51 in Tables 1 and 2), the characteristics of the 1980 earthquake ( $M_w \sim 6.9$ ) can be  
289 used to evaluate  $M_{max}$  via comparison with the  $M_{max}$  derived from scaling  
290 relationships. In such cases, we (i) calculated the maximum expected magnitude



291 ( $M_{max1}$ ) and the relative uncertainties using only the scaling relationships and (ii)  
 292 compared the maximum of observed magnitudes of the earthquakes potentially  
 293 associated with the fault. If MObs was within the range of  $M_{max} \pm 1$  standard  
 294 deviation, we considered the value and recalculated a new  $M_{max}$  ( $M_{max2}$ ) with a new  
 295 uncertainty. If MObs was larger than  $M_{max1}$ , we reviewed the fault geometry and/or  
 296 the earthquake-source association.

297 Because all the empirical relationships, as well as observed historical and recent  
 298 magnitudes of earthquakes, are affected by uncertainties, the *MomentBalance* (MB)  
 299 portion of the FiSH code (Pace et al., 2016) was used to account for these  
 300 uncertainties. MB computes a probability density function for each magnitude  
 301 derived from empirical relationships or observations and summarizes the results as a  
 302 maximum magnitude value with a standard deviation. The uncertainties in the  
 303 empirical scaling relationship are taken from the studies of Wells and Coppersmith  
 304 (1994), Peruzza and Pace (2002) and Leonard (2010). Currently, the uncertainty in  
 305 magnitude associated with the seismic moment is fixed and set to 0.3, whereas the  
 306 catalogue defines the uncertainty in MObs. Moreover, to combine the evaluated  
 307 maximum magnitudes, MB creates a probability curve for each magnitude by  
 308 assuming a normal distribution (Fig. 2). We assumed an untruncated normal  
 309 distribution of magnitudes at both sides. MB successively sums the probability  
 310 density curves and fits the summed curve to a normal distribution to obtain the mean  
 311 of the maximum magnitude  $M_{max}$  and its standard deviation.

312 Thus, a unique  $M_{max}$  with a standard deviation is computed for each source, and this  
 313 value represents the maximum rupture that is allowed by the fault geometry and the  
 314 rheological properties.

315 Finally, to obtain the mean recurrence time of  $M_{max}$  (i.e.,  $T_{mean}$ ), we use the criterion  
 316 of “segment seismic moment conservation” proposed by Field et al. (1999). This  
 317 criterion divides the seismic moment that corresponds to  $M_{max}$  by the moment rate  
 318 for given a slip rate:

$$319 T_{mean} = \frac{1}{Char\_Rate} = \frac{10^{1.5} M_{max}^{9.1}}{\mu VLW} \quad (1)$$

320 where  $T_{mean}$  is the mean recurrence time in years,  $Char\_Rate$  is the annual mean  
321 rate of occurrence,  $M_{max}$  is the computed mean maximum magnitude,  $\mu$  is the shear  
322 modulus,  $V$  is the average long-term slip rate, and  $L$  and  $W$  are ~~geometrical~~  
323 ~~parameters of the fault~~ along-strike ruptur~~length~~ and downdip width, respectively.  
324 This approach was used for ~~both MFDs~~ in this study, and, in particular, we evaluated  
325  $M_{max}$  and  $T_{mean}$  based on the fault geometry and the slip rate of each individual  
326 source. Additionally, ~~we calculated the total expected seismic moment rate using~~  
327 ~~equation 1~~. Then, we partitioned the total expected seismic moment rate based on a  
328 range given by  $M_{max} \pm 1$  standard deviation following a Gaussian distribution.  
329 After the fault source is entered as input, the seismic moment rate is calculated,  $M_{max}$   
330 (*Fig. 2b*) and  $T_{mean}$  are defined for each source, we computed the MFDs of expected  
331 seismicity. For each fault source, we use two “end-member” MFD models: (i) a  
332 *Characteristic Gaussian (CHG)* model, a symmetric Gaussian curve (applied to the  
333 incremental MFD values) centred on the  $M_{max}$  value of each fault with a range of  
334 magnitudes equal to 1-sigma, and (ii) a *Truncated Gutenberg-Richter (TGR, Ordaz,*  
335 *1999; Kagan, 2002*) model, with  $M_{max}$  as the upper threshold and  $M_w = 5.5$  as the  
336 minimum threshold for all sources. The ~~b-values are constant and equal to 1.0 for all~~  
337 ~~faults, and they are obtained by the interpolation of earthquake data from~~ the CPTI15  
338 catalogue, as single-source events are insufficient for calculating the required  
339 statistics. The a-values were computed with the *ActivityRate* tool of the *FiSH* code.  
340 *ActivityRate* balances the total expected seismic moment rate with the seismic  
341 ~~moment rate that was obtained based on  $M_{max}$  and  $T_{mean}$~~  (details in Pace et al.,  
342 2016). In *Figure 2c*, we show an example of the expected seismicity rates in terms of  
343 the annual cumulative rates for the Paganica source using the two above-described  
344 ~~MFDs~~.  
345 Finally, we create a so-called “expert judgement” model, called the *Mixed* model, to  
346 determine the MFD for each fault source based on the earthquake-source  
347 associations. In this case, we decided that if an earthquake assigned to a fault  
348 source (see *Table 2* for earthquake-source associations) has a magnitude lower than  
349 the magnitude range in the curve of the *CHG* model distribution, the *TGR* model is  
350 applied to that fault source. Otherwise, the *CHG* model, which peaks at the  
351 calculated  $M_{max}$ , is applied. Of course, errors in this approach can originate from the  
352 misallocation of historical earthquakes, and we cannot exclude the possibility that  
353 potentially active faults responsible for historical earthquakes have not yet been

354 mapped. The MFD model assigned to each fault source in our *Mixed* model is shown  
355 in Figure 3.

356

357 **2.2 Distributed Source Inputs**

358 Introducing distributed earthquakes into the PSH model is necessary because  
359 researchers have not been able to identify a causative source (i.e., a mapped fault)  
360 for important earthquakes in the historical catalogue. This lack of correlation between  
361 earthquakes and faults may be related to (i) interseismic strain accumulation in areas  
362 between major faults, (ii) earthquakes occurring on unknown or blind faults, (iii)  
363 earthquakes occurring on unmapped faults characterized by slip rates lower than the  
364 rates of erosional processes, and/or (iv) the general lack of surface ruptures  
365 associated with faults generating  $M_w < 5.5$  earthquakes.

366 We used the historical catalogue of earthquakes (CPTI15; Rovida et al., 2016; Fig.  
367 4) to model the occurrence of moderate-to-large ( $M_w \geq 4.5$ ) earthquakes. The  
368 catalogue consists of 4,427 events and covers approximately the last one thousand  
369 years from 01/01/1005 to 28/12/2014. Before using the catalogue, we removed all  
370 events not considered mainshocks via a declustering filter (Gardner and Knopoff,  
371 1977). This process resulted in a **complete catalogue** composed of 1,839  
372 independent events. Moreover, to avoid any ~~any artificial effects related to~~ double  
373 counting due to the use of two seismicity sources, i.e., the fault sources and the  
374 distributed seismicity sources, we removed events associated with known active  
375 faults from the CPTI15 earthquake catalogue. If the causative fault of an earthquake  
376 is known, that earthquake does not need to be included in the seismicity smoothing  
377 procedure. The earthquake-source association is based on neotectonics,  
378 palaeoseismology and seismotectonics papers (see the supplemental files) and, in a  
379 few cases, macroseismic intensity maps. In Table 2, we listed the earthquakes with  
380 known causative fault sources. The differences in the smoothed rates given by eq.  
381 (2) using the complete and modified catalogues are shown in Figure 5.

382 We applied the standard methodology developed by Frankel (1995) to estimate the  
383 density of seismicity in a grid with latitudinal and longitudinal spacing of  $0.05^\circ$ . The  
384 smoothed rate of events in each cell  $i$  is determined as follows:

385

$$n_i = \frac{\sum_j n_j e^{-\frac{\Delta_{ij}^2}{c^2}}}{\sum_j e^{-\frac{\Delta_{ij}^2}{c^2}}} \quad (2)$$

386 where  $n_i$  is the cumulative rate of earthquakes with magnitudes greater than the  
 387 completeness magnitude  $Mc$  in each cell  $i$  of the grid and  $\Delta_{ij}$  is the distance between  
 388 the centres of grid cells  $i$  and  $j$ . The parameter  $c$  is the correlation distance. The sum  
 389 is calculated in cells  $j$  within a distance of  $3c$  of cell  $i$ .

390 To compute earthquake rates, we adopted the completeness magnitude thresholds  
 391 over different periods given by Stucchi et al. (2011) for five large zones (Fig. 4).

392 To optimize the smoothing distance  $\Delta$  in eq. (2), we divided the earthquake  
 393 catalogue into four 10-yr disjoint learning and target periods from the 1960s to the  
 394 1990s. For each pair of learning and target catalogues, we used the probability gain  
 395 per earthquake to find the optimal smoothing distance (Kagan and Knopoff, 1977;  
 396 Helmstetter et al., 2007). After assuming a spatially uniform earthquake density  
 397 model as a reference model, the probability gain per earthquake  $G$  of a candidate  
 398 model relative to a reference model is given by the following equation:

399

$$G = \exp\left(\frac{L - L_0}{N}\right) \quad (3)$$

400 where  $N$  is the number of events in the target catalogue and  $L$  and  $L_0$  are the joint  
 401 log-likelihoods of the candidate model and reference model, respectively. Under the  
 402 assumption of a Poisson earthquake distribution, the joint log-likelihood of a model is  
 403 given as follows:

404

$$L = \sum_{i_x=1}^{N_x} \sum_{i_y=1}^{N_y} \log p [\lambda(i_x, i_y), \omega] \quad (4)$$

405 where  $p$  is the Poisson probability,  $\lambda$  is the spatial density,  $\omega$  is the number of  
 406 observed events during the target period, and the parameters  $i_x$  and  $i_y$  denote each  
 407 corresponding longitude-latitude cell.

408 Figure 6 shows that for the four different pairs of learning-target catalogues, the  
 409 optimal smoothing distance  $c$  ranges from 30-40 km. Finally, the mean of all the

410 probability gains per earthquake yields a maximum smoothing distance of 30 km  
411 (Fig. 6), which is then used in eq. (2).

412 The b-value of the GR distribution is calculated on a regional basis using the  
413 maximum-likelihood method of Weichert (1980), which allows multiple periods with  
414 varying completeness levels to be combined. Following the approach recently  
415 proposed by Kamer and Hiemer (2015), we used a penalized likelihood-based  
416 method for the spatial estimation of the GR b-values based on the Voronoi  
417 tessellation of space without tectonic dependency. The whole Italian territory has  
418 been divided into a grid with a longitude/latitude spacing of 0.05°, and the centres of  
419 the grid cells represent the possible centres of Voronoi polygons. We vary the  
420 number of Voronoi polygons,  $N_v$ , from 3 to 50, generating 1000 tessellations for  
421 each  $N_v$ . The summed log-likelihood of each obtained tessellation is compared with  
422 the log-likelihood given by the simplest model (prior model) obtained using the entire  
423 earthquake dataset. We find that 673 random realizations led to better performance  
424 than the prior model. Thus, we calculate an ensemble model using these 673  
425 solutions, and the mean b-value of each grid node is shown in Figure 4.

426 The maximum magnitude  $M_{max}$  assigned to each node of the grid, the nodal planes  
427 and the depths have been taken from the SHARE European project (Woessner et  
428 al., 2015). The SHARE project evaluated the maximum magnitudes of large areas of  
429 Europe based on a joint procedure involving historical observations  tectonic  
430 regionalization. We adopted the lowest of the **maximum magnitudes** proposed by  
431 SHARE, but evaluating the impact of different maximum magnitudes is beyond the  
432 scope of this work.

433 Finally, the rates of expected seismicity for each node of the grid are assumed to  
434 follow the TGR model (Kagan 2002):

435 
$$\lambda(M) = \lambda_0 \frac{\exp(-\beta M) - \exp(-\beta M_u)}{\exp(-\beta M_0) - \exp(-\beta M_u)} \quad (5)$$

436 where the magnitude ( $M$ ) is in the range of  $M_0$  (minimum magnitude) to  $M_u$  (upper or  
437 maximum magnitude); otherwise  $\lambda(M)$  is 0. Additionally,  $\lambda_0$  is the smoothed rate of  
438 earthquakes at  $M_w = 4.5$  and  $\beta = b \ln(10)$ .

439 **2.3 Combining Fault and Distributed Sources**

440 To combine the two source inputs, we introduced a distance-dependent linear  
441 weighting function, such that the contribution from the distributed sources linearly  
442 decreases from 1 to 0 with decreasing distance from the fault. The expected  
443 seismicity rates of the distributed sources start at  $Mw = 4.5$ , which is lower than the  
444 minimum magnitude of the fault sources, and the weighting function is only  
445 applicable in the magnitude range overlapping the MFD of each fault. This weighting  
446 function is based on the assumption that faults tend to modify the surrounding  
447 deformation field (Fig. 7), and this assumption is explained in detail later in this  
448 paper.

449 During fault system evolution, the increase in the size of a fault through linking with  
450 other faults results in an increase in displacement that is proportional to the quantity  
451 of strain accommodated by the fault (Kostrov, 1974). Under a constant regional  
452 strain rate, the activity of ~~arranged across strike~~ must eventually decrease (Nicol et  
453 al., 1997; Cowie, 1998; Roberts et al., 2004). Using ~~an~~ analogue modelling,  
454 Mansfield and Cartwright (2001) showed that faults grow via cycles of overlap, relay  
455 formation, breaching and linkage between neighbouring segments across a wide  
456 range of scales. During the evolution of a system, the merging of neighbour faults,  
457 mostly along ~~the~~ strike, results in the formation of major faults, which ~~are associated~~  
458 ~~with~~ the majority of displacement. These major faults are surrounded by minor faults,  
459 which ~~are associated with lower degrees~~ of displacement. To highlight the spatial  
460 patterns of major and minor faults, Figures 7a and 7b present diagrams from the  
461 Mansfield and Cartwright (2001) experiment in two different stages: the approximate  
462 midpoint of the sequence and the end of the sequence. Numerical modelling  
463 performed by Cowie et al. (1993) yielded similar evolutionary features for major and  
464 minor faults. The numerical fault simulation of Cowie et al. (1993) was able to  
465 reproduce the development of a normal fault system from the early nucleation stage,  
466 including interactions with adjacent faults, to full linkage and the formation of a large  
467 ~~through~~ fault. The model also captures the increase in the displacement rate of a  
468 large linked fault. In Figures 7c and 7d, we focus on two stages of the simulation  
469 (from Cowie et al., 1993): the stage in which the fault segments have formed and  
470 some have become linked and the final stage of the simulation.

471 Notably, the spatial distributions of major and minor faults are very similar in the  
472 experiments of both Mansfield and Cartwright (2001) and Cowie et al. (1993), as  
473 shown in Figures 7a-d. Developments during the early stage of major fault formation  
474 appear to control the location and evolution of future faults, with some areas where  
475 no major faults develop. The long-term evolution of a fault system is the  
476 consequence of the progressive cumulative effects of the slip history, i.e.,  
477 earthquake occurrence, of each fault. Large earthquakes are generally thought to  
478 produce static and dynamic stress changes in the surrounding areas (King et al.,  
479 1994; Stein, 1999; Pace et al., 2014; Verdecchia and Carena, 2016). Static stress  
480 changes produce areas of negative stress, also known as shadow zones, and  
481 positive stress zones. The spatial distributions of decreases (unloading) and  
482 increases (loading) in stress during the long-term slip history of faults likely influence  
483 the distance across strike between major faults. Thus, given a known major active  
484 fault geometrically capable of hosting a  $Mw \geq 5.5$  earthquake, the possibility that a  
485 future  $Mw \geq 5.5$  earthquake will occur in the vicinity of the fault, but is not caused by  
486 that fault, should decrease as the distance from the fault decreases. Conversely,  
487 earthquakes with magnitudes lower than 5.5 and those due to slip along minor faults  
488 are likely to occur everywhere within a fault system, including in proximity to a major  
489 fault.

490 In Figure 7e, we illustrate the results of the analogue and numerical modelling of  
491 fault system evolution and indicate the areas around major faults where it is unlikely  
492 that other major faults develop. In Figure 7f, we show the next step in moving from  
493 geologic and structural considerations. In this step, we combine fault sources and  
494 distributed seismicity source inputs, which serve as inputs for the PSH model. Fault  
495 sources are used to model major faults and are represented by a master fault (i.e.,  
496 one or more major faults) and its projection at the surface. Distributed seismicity is  
497 used to model seismicity associated with minor, unknown or unmapped faults.  
498 Depending on the positions of distributed seismicity points with respect to the buffer  
499 zones around major faults, the rates of expected distributed seismicity remain  
500 unmodified or decrease and can even reach zero.

501 Specifically, we introduced a slip rate and a distance-weighted linear function based  
502 on the above reasoning. The probability of the occurrence of an earthquake ( $P_e$ ) with  
503 a  $Mw$  greater than or equal to the minimum magnitude of the fault is as follows:

504

$$Pe = \begin{cases} 0, & d \leq 1 \text{ km} \\ d/d_{max}, & 1 \text{ km} < d \leq d_{max} \\ 1, & d > d_{max} \end{cases} \quad (6)$$

505 where  $d$  is the Joyner-Boore distance from a fault source. The maximum value of  $d$   
 506 ( $d_{max}$ ) is controlled by the slip rate of the fault. For faults with slip rates  $\geq 1$  mm/yr, we   
 507 assume  $d_{max} = L/2$  ( $L$  is the length along the strike, Fig. 2a); for faults with slip rates  
 508 of 0.3 - 1 mm/yr,  $d_{max} = L/3$ ; and for faults with slip rates of  $\leq 0.3$  mm/yr,  $d_{max} = L/4$ .  
 509 The rationale for varying  $d_{max}$  is given by a simple assumption: the higher the slip  
 510 rate is, the larger the deformation field and the higher the value of  $d_{max}$ . We applied  
 511 eq. (6) to the smoothed occurrence rates of the distributed seismogenic sources.  
 512 Because we consider two fault source inputs, one using only TGR MFD and the  
 513 other only CHR MFD, and because the MFDs of distributed seismicity grid points in  
 514 the vicinity of faults are modified with respect to the MFDs of these faults, we obtain  
 515 two different inputs of distributed seismicity. These two distributed seismogenic  
 516 source inputs differ because the minimum magnitude of the faults is Mw 5.5 in the  
 517 TGR model, but this value depends on each fault source dimension in the CHG  
 518 model, as shown in Figure 8.

519 Our approach allows incompleteness in the fault database to be bypassed, which is  
 520 advantageous because all fault databases should be considered incomplete. In our  
 521 approach, the seismicity is modified only in the vicinity of mapped faults. The  
 522 remaining areas are fully described by the *distributed input*. With this approach, we  
  
 523 do not define areas with reliable fault information, and the locations of currently  
 524 unknown faults can be easily included when they are discovered in the future.

525 **3. Results and Discussion**

526 To obtain PSH maps, we assign the calculated seismicity rates, based on the  
 527 Poisson hypothesis, to their pertinent geometries, i.e., individual 3D seismogenic   
 528 sources for the *fault input* and point sources for the *distributed input* (Fig. 8). All the  
 529 computations are performed using the OpenQuake Engine (Global Earthquake  
 530 Model, 2016) with a grid spacing of 0.05° in both latitude and longitude. We use  this  
 531 software because it is open source software developed recently by GEM with the  
 532 purpose of providing seismic hazard and risk assessments. Moreover, it is widely  
 533 recognized within the scientific community for its potential. The ground motion

534 prediction equations (GMPE) of Akkar et al. (2013), Chiou et al. (2008), Faccioli et  
535 al., (2010) and Zhao et al., (2006) are used, as suggested by the SHARE European  
536 project (Woessner et al., 2015). In addition, we used the GMPE proposed by Bindi et  
537 al. (2014) and calibrated using Italian data. We combined all GMPEs into a logic tree  
538 with the same weight of 0.2 for each branch. The distance used for each GMPE was  
539 the Joyner and Boore distance for Akkar et al. (2013), Bindi et al. (2014) and Chiou  
540 et al. (2008) and the closest rupture distance for Faccioli et al. (2010) and Zhao et al.  
541 (2006).

542 The results of the fault source inputs, distributed source inputs, and aggregated  
543 model are expressed in terms of peak ground acceleration (PGA) based on  
544 exceedance probabilities of 10% and 2% over 50 years, corresponding to return  
545 periods of 475 and 2,475 years, respectively (Fig. 9).

546 To explore the epistemic uncertainty associated with the distribution of activity rates  
547 over the range of magnitudes of fault source inputs, we compared the seismic  
548 hazard levels obtained based on the TGR and CHG fault source inputs (left column  
549 in Fig. 9) using the TGR and CHG MFDs for all the fault sources (details in section  
550 2.1.3). Although both models have the same seismic moment release, the different  
551 MFDs generate clear differences. In fact, in the TGR model, all faults contribute  
552 significantly to the seismic hazard level, whereas in the CHG model, only a few faults  
553 located in the central Apennines and Calabria contribute to the seismic hazard level.  
554 This difference is due to the different shapes of the MFDs in the two models (Fig.  
555 2c). As shown in Figure 8, the percentage of earthquakes with magnitudes between  
556 5.5 and approximately 6, which are likely the main contributors to these levels of  
557 seismic hazards, is generally higher in the TGR model than in the CHG model. At a  
558 2% probability of exceedance in 50 years, all fault sources in the CHG contribute to  
559 the seismic hazard level, but the absolute values are still generally higher in the TGR  
560 model.

561 The *distributed input* (middle column in Fig. 9) depicts a more uniform shape of the  
562 seismic hazard level than that of fault source inputs. A low PGA value of 0.125 g at a  
563 10% probability of exceedance over 50 years and a low value of 0.225 g at a 2%  
564 probability of exceedance over 50 years encompass a large part of peninsular Italy

565 and Sicily. Two areas with high seismic hazard levels are located in the central  
566 Apennines and northeastern Sicily.

567 The overall model, which was ~~created~~ by combining the fault and distributed source  
568 inputs, is shown in the right column of Figure 9. Areas with comparatively high  
569 seismic hazard levels, i.e., hazard levels greater than 0.225 g and greater than 0.45  
570 g at 50-yr exceedance probabilities of 10% and 2%, respectively, are located  
571 throughout the Apennines, in Calabria and in Sicily. The fault source inputs  
572 contribute most to the total seismic hazard levels in the Apennines, Calabria and  
573 eastern Sicily, where the highest PGA values are observed.



574 Figure 10 shows the **contributions to** the total seismic hazard level by the *fault* and  
575 *distributed* source inputs at a specific site (L'Aquila, 42.400-13.400). Notably, in  
576 Figure 10, *distributed* sources dominate the seismic hazard contribution at  
577 exceedance probabilities greater than ~81% over 50 years, but the contribution of  
578 *fault* sources cannot be neglected. Conversely, at exceedance probabilities of less  
579 than ~10% in 50 years, the total hazard level is mainly associated with *fault* source  
580 inputs.

581 Figure 11 presents seismic hazard maps for ~~PGAs~~ at 10% and 2% exceedance  
582 probabilities in 50 years for *fault* sources, *distributed* sources and a combination of  
583 the two. These data were obtained using the above-described *Mixed* model, in which  
584 we selected the most “appropriate” MFD model (TGR or CHG) for each fault (as  
585 shown in Figure 3). The results of this model therefore have values between those of  
586 the two end-members shown in Figure 9.

587 Figure 12 shows the *CHG*, *TGR* and *Mixed* model hazard curves of three sites  
588 (Cesena, L'Aquila and Crotone, Fig. 13c). As previously noted, the results of the  
589 *Mixed* model, due to the structure of the model, are between those of the *CHG* and  
590 *TGR* models. The relative positions of the hazard curves derived from the two end-  
591 member models and the *Mixed* model depend on the number of nearby fault sources  
592 that have been modelled using one of the MFD models and on the distance of the  
593 site from the faults. For example, in the case of the Crotone site, the majority of the  
594 fault sources in the *Mixed* model are modelled using the CHG MFD. Thus, the  
595 resulting hazard curve is similar to that of the *CHG* model. For the Cesena site, the

596 three hazard curves overlap. Because the distance between Cesena and the closest  
597 fault sources is approximately 60 km, the impact of the fault input is less than the  
598 impact of the *distributed* source input. In this case, the choice of a particular MFD  
599 model has a limited impact on the modelling of *distributed* sources. Notably, for an  
600 annual frequency of exceedance (AFOE) lower than  $10^{-4}$ , the *TGR fault* source input  
601 values are generally higher than those of the *CHG* source input, and the three  
602 models converge at  $AFOE < 10^{-4}$ . The resulting seismic hazard estimates depend on  
603 the assumed MFD model (*TGR* vs. *CHG*), especially for intermediate-magnitude  
604 events (5.5 to  $\sim$ 6.5). Because we assume that the maximum magnitude is imposed  
605 by the fault geometry and that the seismic moment release is controlled by the slip  
606 rate, the *TGR* model leads to the highest hazard values because this range of  
607 magnitude contributes the most to the hazard level. 

608 In Figure 13, we investigated the influences of the Mixed *fault* source inputs and the  
609 Mixed *distributed* source inputs on the total hazard level of the entire study area, as  
610 well as the ~~variability in the hazard results~~. The maps in Figure 13a show that the  
611 contribution of *fault* inputs to the total hazard level generally decreases as the  
612 exceedance probability increases from 2% to 81% in 50 years. At a 2% probability of  
613 exceedance in 50 years, the total hazard levels in the Apennines and eastern Sicily  
614 are mainly related to faults, whereas at an 81% probability of exceedance in 50  
615 years, the contributions of *fault* inputs are high in local areas of central Italy and  
616 southern Calabria.

617 Moreover, we examined the contributions of *fault* and *distributed* sources along three  
618 E-W-oriented profiles in northern, central and southern Italy (Fig. 13b). Note that the  
619 contributions are not based on deaggregation but are computed according to the  
620 percentage of each source input in the AFOE value of the combined model. In areas  
621 with faults, the hazard level estimated by *fault* inputs is generally higher than that  
622 estimated by the corresponding *distributed* source inputs. Notable exceptions are  
623 present in areas proximal to slow-slipping active faults at an 81% probability of  
624 exceedance in 50 years (profile A), such as those at the eastern and western  
625 boundaries of the fault area in central Italy (profile B), and in areas where the  
626 contribution of the *distributed* source input is equal to that of the *fault* input at a 10%  
627 probability of exceedance in 50 years (eastern part of profile C). 

628 The features depicted by the three profiles result from a combination of the slip rates  
629 and spatial distributions of faults for *fault* source inputs. This pattern should be  
630 considered a critical aspect of using fault models for PSH analysis. In fact, the  
631 proposed approach requires a high level of expertise in active tectonics and cautious  
632 expert judgement at many levels in the procedure. First, the seismic hazard estimate  
633 is based on the definition of a segmentation model, which requires a series of rules  
634 based on observations and empirical regression between earthquakes and the size  
635 of the causative fault. New data might make it necessary to revise the rules or  
636 reconsider the role of the segmentation. In some cases, expert judgement could  
637 permit discrimination among different fault source models. Alternatively, all models  
638 should be considered branches in a logic tree approach.

639 Moreover, we propose a fault seismicity input in which the MFD of each fault source  
640 has been chosen based on an analysis of the occurrences of earthquakes that can  
641 be tentatively or confidently assigned to a certain fault. To describe the fault activity,  
642 we applied a probability density function to the magnitude, as commonly performed  
643 in the literature: the TGR model, where the maximum magnitude is the upper  
644 threshold and  $M_w = 5.5$  is the lower threshold for all faults, and the characteristic  
645 maximum magnitude model, which consists of a truncated normal distribution  
646 centred on the maximum magnitude. Other MFDs have been proposed to model the  
647 earthquake recurrence of a fault. For example, Youngs and Coppersmith (1985)  
648 proposed a modification to the truncated exponential model to allow for the  
649 increased likelihood of characteristic events. However, we focused only on two  
650 models, as we believe that instead of a “blind” or qualitative characterization of the  
651 MFD of a fault source, future applications of statistical tests of the compatibility  
652 between expected earthquake rates and observed historical seismicity could be used  
653 as an objective method of identifying the optimal MFD of expected seismicity.

654 To focus on the general procedure for spatially integrating faults with sources  
655 representing distributed (or off-fault) seismicity, we did not investigate the impact of  
656 other smoothing procedures on the distributed sources, and we used fixed kernels  
657 with a constant bandwidth (as in the works of Kagan and Jackson, 1994; Frankel et  
658 al. 1997; Zechar and Jordan, 2010). The testing of adaptive bandwidths (e.g., Stock

659 and Smith, 2002; Helmstetter et al., 2006, 2007; Werner et al., 2011) or weighted  
660 combinations of both models has been reserved for future studies.

661

662 Finally, we compared, as shown in Figure 14, the 2013 European Seismic Hazard  
663 Model (ESHM13) developed within the SHARE project, the current Italian national  
664 seismic hazard map (MPS04) and the results of our model (Mixed model) using the  
665 same GMPEs as used in this study. Specifically, for ESHM13, we compared the  
666 results to the fault-based hazard map (FSBG model) that accounts for fault sources  
667 and background seismicity. The figure shows how the impact of our fault sources is  
668 more evident than in FSBG-ESHM13, and the comparison with MPS04 confirms a  
669 similar pattern, but with some significant differences at the regional to local scales.

670

671 The strength of our approach lies in the integration of different levels of information  
672 regarding the active faults in Italy, but the final result is unavoidably linked to the  
673 quality of the relevant data. Our work focused on presenting and applying a new  
674 approach for evaluating seismic hazards based on active faults and intentionally  
675 avoided the introduction of uncertainties due to the use of different segmentation  
676 rules or other slip rate values of faults. Moreover, the impact of ground motion  
677 predictive models is important in seismic hazard assessment but beyond the scope  
678 of this work. Future steps will be devoted to analysing these uncertainties and  
679 evaluating their impacts on seismic hazard estimates.

680

#### 681 **4. Conclusions**

682 We presented our first national-scale PSH model of Italy, which summarizes and  
683 integrates the fault-based PSH models developed since the publication of Pace et al.  
684 in 2006.

685 The model proposed in this study combines fault source inputs based on over 110  
686 faults grouped into 86 fault sources and distributed source inputs. For each fault  
687 source, the maximum magnitude and its uncertainty were derived by applying  
688 scaling relationships, and the rates of seismic activity were derived by applying slip  
689 rates to seismic moment evaluations and balancing these seismic moments using  
690 two MFD models.

691 To account for unknown faults, a distributed seismicity input was applied following  
692 the well-known Frankel (1995) methodology to calculate seismicity parameters.

693 The fault sources and distributed sources have been integrated via a new approach  
694 based on the idea that deformation in the vicinity of an active fault is concentrated  
695 along the fault and that the seismic activity in the surrounding region is reduced. In  
696 particular, a distance-dependent linear weighting function has been introduced to  
697 allow the contribution of distributed sources (in the magnitude range overlapping the  
698 MFD of each fault source) to linearly decrease from 1 to 0 with decreasing distance  
699 from a fault. The strength of our approach lies in the ability to integrate different  
700 levels of available information for active faults that actually exist in Italy (or  
701 elsewhere), but the final result is unavoidably linked to the quality of the relevant  
702 data.

703 The PSH maps produced using our model show a hazard pattern similar to that of  
704 the current maps at the national scale, but some significant differences in hazard  
705 level are present at the regional to local scales (Figure 13).

706 Moreover, the impact ~~that~~ using different MFD models to derive seismic activity rates  
707 ~~has~~ on the hazard maps was investigated. The PGA values in the hazard maps  
708 ~~generated by~~ the *TGR* model are higher than those in the hazard maps ~~generated by~~  
709 the *CHG* model. This difference is because the rates of earthquakes with  
710 magnitudes from 5.5 to approximately 6 are generally higher in the *TGR* model than  
711 in the *CHG* model. Moreover, the relative contributions of fault source inputs and  
712 distributed source inputs have been identified in maps and profiles in three sectors of  
713 the study area. These profiles show that the hazard level is generally higher where  
714 fault inputs are used, and for high probabilities of exceedance, the contribution of  
715 *distributed* inputs equals that of *fault* inputs.

716 Finally, the *Mixed* model was created by selecting the most appropriate MFD model  
717 for each fault. All data, including the locations and parameters of fault sources, are  
718 provided in the supplemental files of this paper.

719 This new PSH model is not intended to replace, integrate or assess the current  
720 official national seismic hazard model of Italy. While some aspects remain to be  
721 implemented in our approach (e.g., the integration of reverse/thrust faults in the  
722 database, sensitivity tests for the distance-dependent linear weighting function  
723 parameters, sensitivity tests for potential different segmentation models, and fault  
724 source inputs that account for fault interactions), the proposed model represents

725 advancements in terms of input data (quantity and quality) and methodology based  
726 on a decade of research in the field of fault-based approaches to regional seismic  
727 hazard modelling.

728

729

730

731

732

733

734

735 **References**

736

737

738 Akinci, A., Galadini, F., Pantosti, D., Petersen, M., Malagnini, L., and Perkins, D.:  
739 Effect of Time Dependence on Probabilistic Seismic-Hazard Maps and  
740 Deaggregation for the Central Apennines, Italy, B Seismol Soc Am, 99, 585-  
741 610, 2009.

742 Akkar, S., Sandikkaya, M.A. , Bommer, J.J.: Empirical Ground-Motion Models for  
743 Point and Extended-Source Crustal Earthquake Scenarios in Europe and the  
744 Middle East, Bulletin of Earthquake Engineering, ISSN:1570-761X, 2013.

745 Basili, R., Valensise, G., Vannoli, P., Burrato, P., Fracassi, U., Mariano, S., Tiberti,  
746 M. M. and Boschi, E.: The Database of Individual Seismogenic Sources  
747 (DISS), version 3: Summarizing 20 years of research on Italy's earthquake  
748 geology, Tectonophysics, 453, 20- 43, 2008.

749 Benedetti, L., Manighetti, I., Gaudemer, Y., Finkel, R., Malavieille, J., Pou, K., Arnold,  
750 M., Aumaitre, G., Bourles, D., and Keddadouche, K.: Earthquake synchrony  
751 and clustering on Fucino faults (Central Italy) as revealed from in situ Cl-36  
752 exposure dating, J Geophys Res-Sol Ea, 118, 4948-4974, 2013.

753 Bindi, D., Massa, M., Luzi, L., Ameri, G., Pacor, F., Puglia, R., and Augliera, P.: Pan-  
754 European ground-motion prediction equations for the average horizontal  
755 component of PGA, PGV, and 5%-damped PSA at spectral periods up to 3.0  
756 s using the RESORCE dataset (vol 12, pg 391, 2014), B Earthq Eng, 12, 431-  
757 448, 2014.

758 Boncio, P., Brozzetti, F. and Lavecchia G.: Architecture and seismotectonics of a  
759 regional Low-Angle Normal Fault zone in Central Italy. *Tectonics*, 19 (6),  
760 1038-1055, 2000.

761 Boncio, P., Lavecchia, G., and Pace, B.: Defining a model of 3D seismogenic  
762 sources for Seismic Hazard Assessment applications: The case of central  
763 Apennines (Italy), *J Seismol*, 8, 407-425, 2004.

764 Boncio, P., Pizzi, A., Cavuoto, G., Mancini, M., Piacentini, T., Miccadei, E., Cavinato,  
765 G. P., Piscitelli, S., Giocoli, A., Ferretti, G., De Ferrari, R., Gallipoli, M. R.,  
766 Mucciarelli, M., Di Fiore, V., Franceschini, A., Pergalani, F., Naso, G., and  
767 Macroarea, W. G.: Geological and geophysical characterisation of the  
768 Paganica - San Gregorio area after the April 6, 2009 L'Aquila earthquake (M-  
769 w 6.3, central Italy): implications for site response, *B Geofis Teor Appl*, 52,  
770 491-512, 2011.

771 Bull, J. M., Barnes, P. M., Lamarche, G., Sanderson, D. J., Cowie, P. A., Taylor, S.  
772 K., and Dix, J. K.: High-resolution record of displacement accumulation on an  
773 active normal fault: implications for models of slip accumulation during  
774 repeated earthquakes, *J Struct Geol*, 28, 1146-1166, 2006.

775 Chiou, B. S. J. and Youngs, R. R.: An NGA model for the average horizontal  
776 component of peak ground motion and response spectra, *Earthq Spectra*, 24,  
777 173-215, 2008.

778 Cornell, C.A.: Engineering seismic risk analysis, *Bull. Seism. Soc. Am.*, 58, 1583-  
779 1606, 1968.

780 Cowie, P. A.: A healing-reloading feedback control on the growth rate of seismogenic  
781 faults, *J Struct Geol*, 20, 1075-1087, 1998.

782 Cowie, P. A., Roberts, G. P., Bull, J. M., and Visini, F.: Relationships between fault  
783 geometry, slip rate variability and earthquake recurrence in extensional  
784 settings, *Geophys J Int*, 189, 143-160, 2012.

785 Cowie, P. A., Underhill, J. R., Behn, M. D., Lin, J., and Gill, C. E.: Spatio-temporal  
786 evolution of strain accumulation derived from multi-scale observations of Late  
787 Jurassic rifting in the northern North Sea: A critical test of models for  
788 lithospheric extension, *Earth Planet Sc Lett*, 234, 401-419, 2005.

789 Cowie, P. A., Vanneste, C., and Sornette, D.: Statistical Physics Model for the  
790 Spatiotemporal Evolution of Faults, *J Geophys Res-Sol Ea*, 98, 21809-21821,  
791 1993.

792 D'amato, D., Pace, B., Di Nicola, L., Stuart, F.M., Visini, F., Azzaro, R., Branca, S.,  
793 and Barfod, D.N.: Holocene slip rate variability along the Pernicana fault  
794 system (Mt. Etna, Italy): Evidence from offset lava flows: *GSA Bulletin*,  
795 doi:10.1130/B31510.1, 2016.

796 Faccioli, E., Bianchini, A., and Villani, M.: New ground motion prediction equations  
797 for  $t > 1$  s and their influence on seismic hazard assessment, In: *Proceedings*  
798 of the University of Tokyo symposium on long-period ground motion and  
799 urban disaster mitigation, 2010.

800 Ferranti, L., Palano, M., Cannavo, F., Mazzella, M. E., Oldow, J. S., Gueguen, E.,  
801 Mattia, M., and Monaco, C.: Rates of geodetic deformation across active  
802 faults in southern Italy, *Tectonophysics*, 621, 101-122, 2014.

803 Field, E. H., Biasi, G. P., Bird, P., Dawson, T. E., Felzer, K. R., Jackson, D. D.,  
804 Johnson, K. M., Jordan, T. H., Madden, C., Michael, A. J., Milner, K. R., Page,  
805 M. T., Parsons, T., Powers, P. M., Shaw, B. E., Thatcher, W. R., Weldon, R.  
806 J., and Zeng, Y. H.: Long-Term Time-Dependent Probabilities for the Third  
807 Uniform California Earthquake Rupture Forecast (UCERF3), *B Seismol Soc  
808 Am*, 105, 511-543, 2015.

809 Field, E. H., Jackson, D. D., and Dolan, J. F.: A mutually consistent seismic-hazard  
810 source model for southern California, *B Seismol Soc Am*, 89, 559-578, 1999.

811 Finnegan, N. J., Schumer, R., and Finnegan, S.: A signature of transience in bedrock  
812 river incision rates over timescales of 10(4)-10(7) years, *Nature*, 505, 391-+,  
813 2014.

814 Frankel, A.: Simulating Strong Motions of Large Earthquakes Using Recordings of  
815 Small Earthquakes - the Loma-Prieta Mainshock as a Test-Case, *B Seismol  
816 Soc Am*, 85, 1144-1160, 1995.

817 Frankel, A., Mueller, C., Barnhard, T., Perkins, D., Leyendecker, E. V., Dickman, N.,  
818 Hanson, S.. and Hopper, M.: Seismic-hazard maps for California, Nevada,  
819 and Western Arizona/Utah', *U.S. Geological Survey Open-File Rept.* 97-130,  
820 1997.

821 Gallen, S. F., Pazzaglia, F. J., Wegmann, K. W., Pederson, J. L., and Gardner, T.  
822 W.: The dynamic reference frame of rivers and apparent transience in incision  
823 rates, *Geology*, 43, 623-626, 2015.

824 Garcia-Mayordomo, J., Gaspar-Escribano, J. M., and Benito, B.: Seismic hazard  
825 assessment of the Province of Murcia (SE Spain): analysis of source  
826 contribution to hazard, *J Seismol*, 11, 453-471, 2007.

827 Gardner, J. K., Knopoff, L.: Is the sequence of earthquakes in Southern California,  
828 with aftershocks removed, Poissonian?'. *Bulletin of the Seismological Society*  
829 of America, 64, 1363-1367, 1974.

830 Gardner, T. W., Jorgensen, D. W., Shuman, C., and Lemieux, C. R.: Geomorphic  
831 and Tectonic Process Rates - Effects of Measured Time Interval, *Geology*, 15,  
832 259-261, 1987.

833 Gasperini P., Bernardini F., Valensise G. and Boschi E.: Defining Seismogenic  
834 Sources from Historical Earthquake Felt Reports, *Bull. Seism. Soc. Am.*, 89,  
835 94-110, 1999.

836 GEM: The OpenQuake-engine User Manual. Global Earthquake Model (GEM)  
837 Technical Report, doi: 10.13117/GEM.OPENQUAKE.MAN.ENGINE.1.9/01,  
838 189 pages, 2016.

839 Gunderson, K. L., Anastasio, D. J., Pazzaglia, F. J., and Picotti, V.: Fault slip rate  
840 variability on 10(4)-10(5)yr timescales for the Salsomaggiore blind thrust fault,  
841 Northern Apennines, Italy, *Tectonophysics*, 608, 356-365, 2013.

842 Hanks, T. C., and Kanamori, H.: A moment magnitude scale, *Journal of Geophysics*  
843 Research, 84, 2348–2350, 1979.

844 Helmstetter, A., Kagan, Y. Y., and Jackson, D. D.: Comparison of short-term and  
845 time-independent earthquake forecast models for southern California, *B  
846 Seismol Soc Am*, 96, 90-106, 2006.

847 Helmstetter, A., Kagan, Y. Y., and Jackson, D. D.: High-resolution time-independent  
848 grid-based forecast for  $M \leq 5$  earthquakes in California, *Seismol Res Lett*,  
849 78, 78-86, 2007.

850 International Association of Seismology and Physics of the Earth's Interior (IASPEI):  
851 Summary of Magnitude Working Group recommendations on standard  
852 procedures for determining earthquake magnitudes from digital data,  
853 <http://www.iaspei.org/>

854 commissions/CSOI/summary\_of\_WG\_recommendations\_2005.pdf (last  
855 accessed December 2015), 2005.

856 Kagan, Y. Y.: Seismic moment distribution revisited: I. Statistical results, *Geophys J*  
857 *Int*, 148, 520-541, 2002.

858 Kagan, Y., and Knopoff, L.: Earthquake risk prediction as a stochastic process,  
859 *Physics of the Earth and Planetary Interiors*, 14, 97–108, 1977.

860 Kagan, Y. Y. and Jackson, D. D.: Long-Term Probabilistic Forecasting of  
861 Earthquakes, *J Geophys Res-Sol Ea*, 99, 13685-13700, 1994.

862 Kamer, Y. and Hiemer, S.: Data-driven spatial b value estimation with applications to  
863 California seismicity: To b or not to b, *J Geophys Res-Sol Ea*, 120, 5191-  
864 5214, 2015.

865 King, G. C. P., Stein, R. S., and Lin, J.: Static Stress Changes and the Triggering of  
866 Earthquakes, *B Seismol Soc Am*, 84, 935-953, 1994.

867 Kostrov, V. V.: Seismic moment and energy of earthquakes, and seismic flow of  
868 rock, *Physic of the Solid Earth*, 1, 23-44, 1974.

869 Leonard, M.: Earthquake fault scaling: Self-consistent relating of rupture length,  
870 width, average displacement, and moment release. *Bulletin of the*  
871 *Seismological Society of America*, 100(5A), 1971- 1988, 2010.

872 Machette, M.N.: Active, capable, and potentially active faults; a paleoseismic  
873 perspective, *J. Geodyn.*, 29, 387–392, 2000.

874 Main, I.: Statistical physics, seismogenesis, and seismic hazard, *Rev Geophys*, 34,  
875 433-462, 1996.

876 Mansfield, C. and Cartwright, J.: Fault growth by linkage: observations and  
877 implications from analogue models, *J Struct Geol*, 23, 745-763, 2001.

878 Meletti, C., Visini, F., D'Amico, V., and Rovida A.: Seismic hazard in central Italy and  
879 the 2016 Amatrice earthquake, *Annals of Geophysics*, 59, doi:10.4401/ag-  
880 7248, 2016.

881 McClymont, A. F., Villamor, P., and Green, A. G.: Assessing the contribution of off-  
882 fault deformation to slip-rate estimates within the Taupo Rift, New Zealand,  
883 using 3-D ground-penetrating radar surveying and trenching, *Terra Nova*, 21,  
884 446-451, 2009a.

885 McClymont, A. F., Villamor, P., and Green, A. G.: Fault displacement accumulation  
886 and slip rate variability within the Taupo Rift (New Zealand) based on trench  
887 and 3-D ground-penetrating radar data, *Tectonics*, 28, 2009b.

888 Nicol, A., Walsh, J., Berryman, K., and Villamor, P.: Interdependence of fault  
889 displacement rates and paleoearthquakes in an active rift, *Geology*, 34, 865-  
890 868, 2006.

891 Nicol, A., Walsh, J., Mouslopoulou, V., and Villamor, P.: Earthquake histories and  
892 Holocene acceleration of fault displacement rates, *Geology*, 37, 911-914,  
893 2009.

894 Nicol, A., Walsh, J. J., Villamor, P., Seebek, H., and Berryman, K. R.: Normal fault  
895 interactions, paleoearthquakes and growth in an active rift, *J Struct Geol*, 32,  
896 1101-1113, 2010.

897 Nicol, A., Walsh, J. J., Watterson, J., and Underhill, J. R.: Displacement rates of  
898 normal faults, *Nature*, 390, 157-159, 1997.

899 Ordaz, M. and Reyes, C.: Earthquake hazard in Mexico City: Observations versus  
900 computations, *B Seismol Soc Am*, 89, 1379-1383, 1999.

901 Pace, B., Bocchini, G. M., and Boncio, P.: Do static stress changes of a moderate-  
902 magnitude earthquake significantly modify the regional seismic hazard? Hints  
903 from the L'Aquila 2009 normal-faulting earthquake (Mw 6.3, central Italy),  
904 *Terra Nova*, 26, 430-439, 2014.

905 Pace, B., Peruzza, L., Lavecchia, G., and Boncio, P.: Layered seismogenic source  
906 model and probabilistic seismic-hazard analyses in central Italy, *B Seismol  
907 Soc Am*, 96, 107-132, 2006.

908 Pace, B., Visini, F., and Peruzza, L.: FiSH: MATLAB Tools to Turn Fault Data into  
909 Seismic-Hazard Models, *Seismol Res Lett*, 87, 374-386, 2016.

910 Peruzza, L., and Pace B.: Sensitivity analysis for seismic source characteristics to  
911 probabilistic seismic hazard assessment in central Apennines (Abruzzo area),  
912 *Bollettino di Geofisica Teorica ed Applicata* 43, 79–100, 2002.

913 Peruzza, L., Pace, B., and Visini, F.: Fault-Based Earthquake Rupture Forecast in  
914 Central Italy: Remarks after the L'Aquila M-w 6.3 Event, *B Seismol Soc Am*,  
915 101, 404-412, 2011.

916 Peruzza, L., Gee, R., Pace, B., Roberts, G., Scotti, O., Visini,F., Benedetti, L., and  
917 Pagani, M.: PSHA after a strong earthquake: hints for the recovery, *Annals of  
918 Geophysics*, 59, doi:10.4401/ag-7257, 2016

919 Roberts, G. P., Cowie, P., Papanikolaou, I., and Michetti, A. M.: Fault scaling  
920 relationships, deformation rates and seismic hazards: an example from the  
921 Lazio-Abruzzo Apennines, central Italy, *J Struct Geol*, 26, 377-398, 2004.

922 Roberts, G. P. and Michetti, A. M.: Spatial and temporal variations in growth rates  
923 along active normal fault systems: an example from The Lazio-Abruzzo  
924 Apennines, central Italy, *J Struct Geol*, 26, 339-376, 2004.

925 Robinson, R., Nicol, A., Walsh, J. J., and Villamor, P.: Features of earthquake  
926 occurrence in a complex normal fault network: Results from a synthetic  
927 seismicity model of the Taupo Rift, New Zealand, *J Geophys Res-Sol Ea*, 114,  
928 2009.

929 Rovida, A., Locati, M., Camassi, R., Lolli, B., and Gasperini P.: CPTI15, the 2015  
930 version of the Parametric Catalogue of Italian Earthquakes. *Istituto Nazionale*  
931 *di Geofisica e Vulcanologia*. doi:<http://doi.org/10.6092/INGV.IT-CPTI15>, 2016.

932 Scotti, O., Clement, C., and Baumont, D.: Seismic hazard for design and verification  
933 of nuclear installations in France: regulatory context, debated issues and  
934 ongoing developments, *B Geofis Teor Appl*, 55, 135-148, 2014.

935 Stein, R. S., King, G. C. P., and Lin, J.: Stress Triggering of the 1994 M=6.7  
936 Northridge, California, Earthquake by Its Predecessors, *Science*, 265, 1432-  
937 1435, 1994.

938 Stirling, M., McVerry, G., Gerstenberger, M., Litchfield, N., Van Dissen, R.,  
939 Berryman, K., Barnes, P., Wallace, L., Villamor, P., Langridge, R., Lamarche,  
940 G., Nodder, S., Reyners, M., Bradley, B., Rhoades, D., Smith, W., Nicol, A.,  
941 Pettinga, J., Clark, K., and Jacobs, K.: National Seismic Hazard Model for  
942 New Zealand: 2010 Update, *B Seismol Soc Am*, 102, 1514-1542, 2012.

943 Stock, C. and Smith, E. G. C.: Adaptive kernel estimation and continuous probability  
944 representation of historical earthquake catalogs, *B Seismol Soc Am*, 92, 904-  
945 912, 2002a.

946 Stock, C. and Smith, E. G. C.: Comparison of seismicity models generated by  
947 different kernel estimations, *B Seismol Soc Am*, 92, 913-922, 2002b.

948 Stucchi, M., Meletti, C., Montaldo, V., Crowley, H., Calvi, G. M., and Boschi, E.:  
949 Seismic Hazard Assessment (2003-2009) for the Italian Building Code, *B*  
950 *Seismol Soc Am*, 101, 1885-1911, 2011.

951 Verdecchia, A. and Carena, S.: Coulomb stress evolution in a diffuse plate boundary:  
952 1400 years of earthquakes in eastern California and western Nevada, USA,  
953 *Tectonics*, 35, 1793-1811, 2016.

954 Visini, F. and Pace, B.: Insights on a Key Parameter of Earthquake Forecasting, the  
955 Coefficient of Variation of the Recurrence Time, Using a Simple Earthquake  
956 Simulator, *Seismol Res Lett*, 85, 703-713, 2014.

957 Weichert, D. H: Estimation of the earthquake recurrence parameters for unequal  
958 observation periods for different magnitudes, *Bulletin of the Seismological  
959 Society of America*, 70, 1337-1346, 1980.

960 Wells, D. L. and Coppersmith, K. J.: New Empirical Relationships among Magnitude,  
961 Rupture Length, Rupture Width, Rupture Area, and Surface Displacement, *B  
962 Seismol Soc Am*, 84, 974-1002, 1994.

963 Werner, M. J., Helmstetter, A., Jackson, D. D., Kagan, Y. Y., and Wiemer, S.:  
964 Adaptively smoothed seismicity earthquake forecasts for Italy, *Ann Geophys-  
965 Italy*, 53, 107-116, 2010.

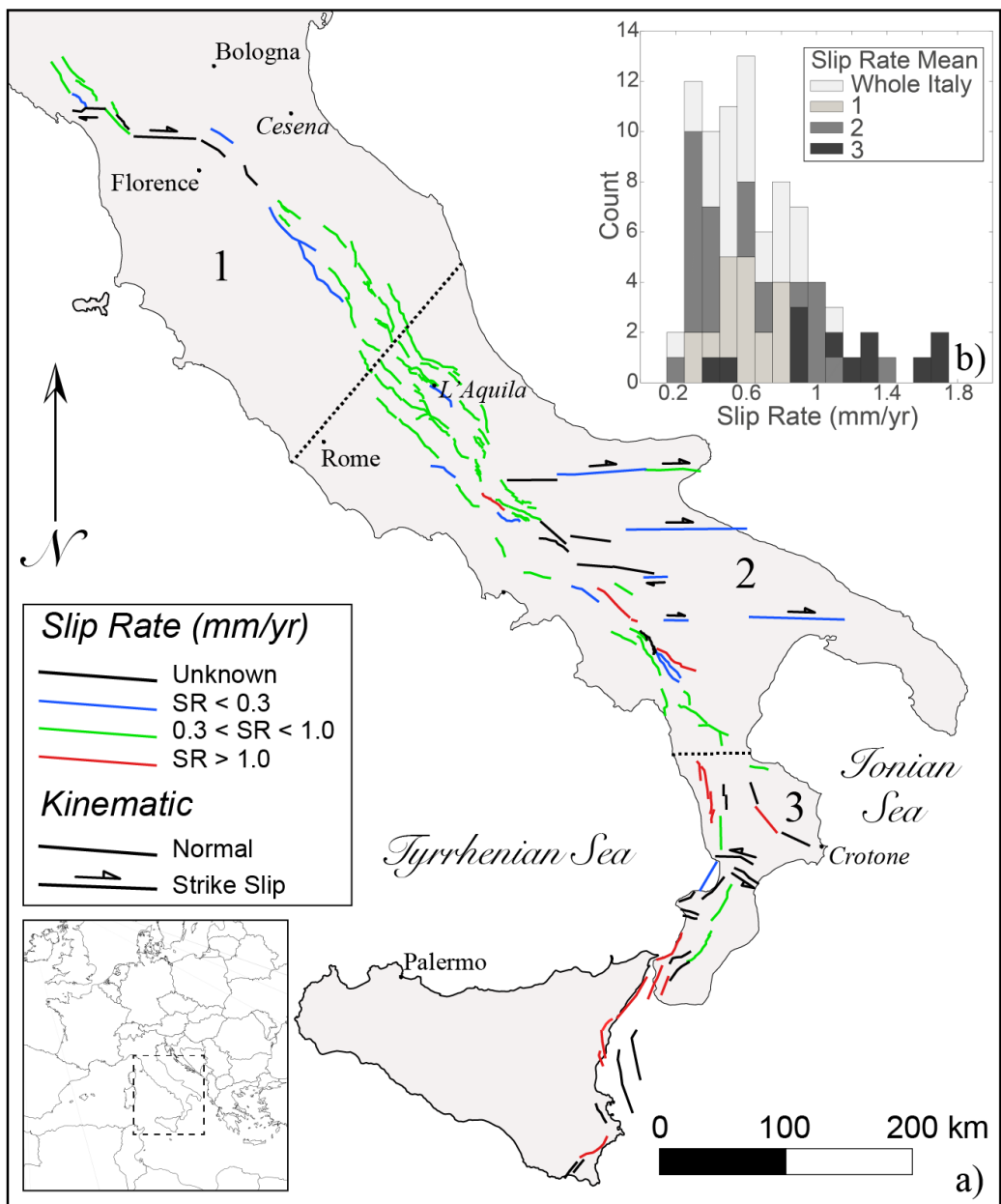
966 Woessner, J., Laurentiu, D., Giardini, D., Crowley, H., Cotton, F., Grunthal, G.,  
967 Valensise, G., Arvidsson, R., Basili, R., Demircioglu, M. B., Hiemer, S.,  
968 Meletti, C., Musson, R. W., Rovida, A. N., Sesetyan, K., Stucchi, M., and  
969 Consortium, S.: The 2013 European Seismic Hazard Model: key components  
970 and results, *B Earthq Eng*, 13, 3553-3596, 2015.

971 Youngs, R. R. and Coppersmith, K. J.: Implications of Fault Slip Rates and  
972 Earthquake Recurrence Models to Probabilistic Seismic Hazard Estimates, *B  
973 Seismol Soc Am*, 75, 939-964, 1985.

974 Zechar, J. D. and Jordan, T. H.: Simple smoothed seismicity earthquake forecasts  
975 for Italy, *Ann Geophys-Italy*, 53, 99-105, 2010.

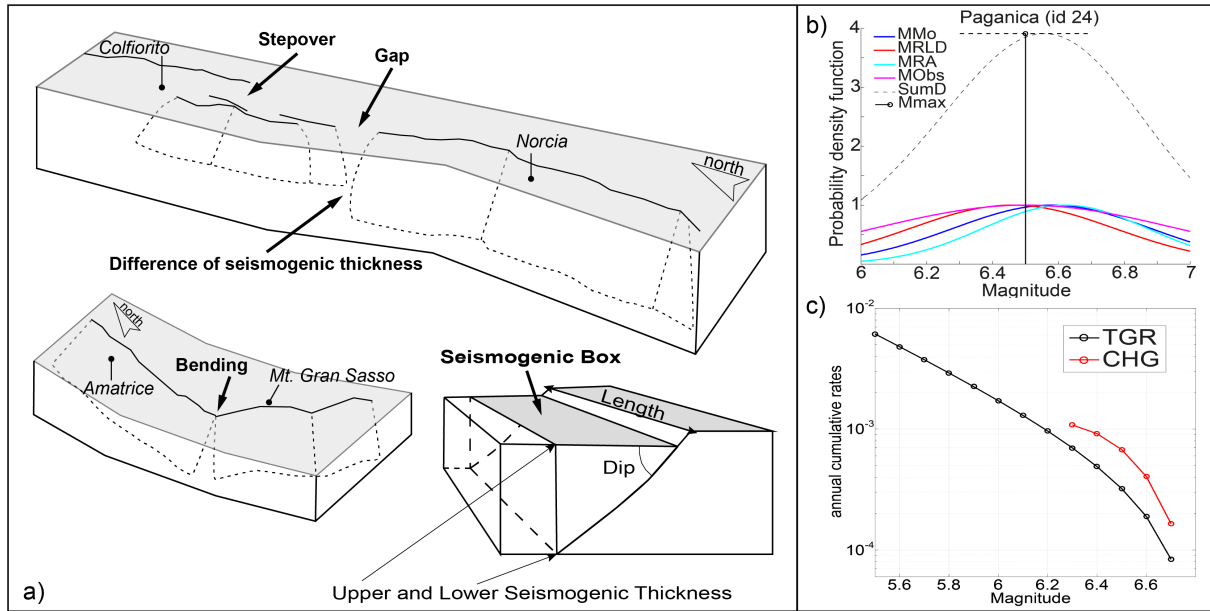
976 Zhao, J. X., Zhang, J., Asano, A., Ohno, Y., Ouchi, T., Takahashi, T., Ogawa, H.,  
977 Irikura, K., Thio, H. K., Somerville, P. G., Fukushima, Y., and Fukushima, Y.:  
978 Attenuation relations of strong ground motion in Japan using site classification  
979 based on predominant period, *B Seismol Soc Am*, 96, 898-913, 2006.

980



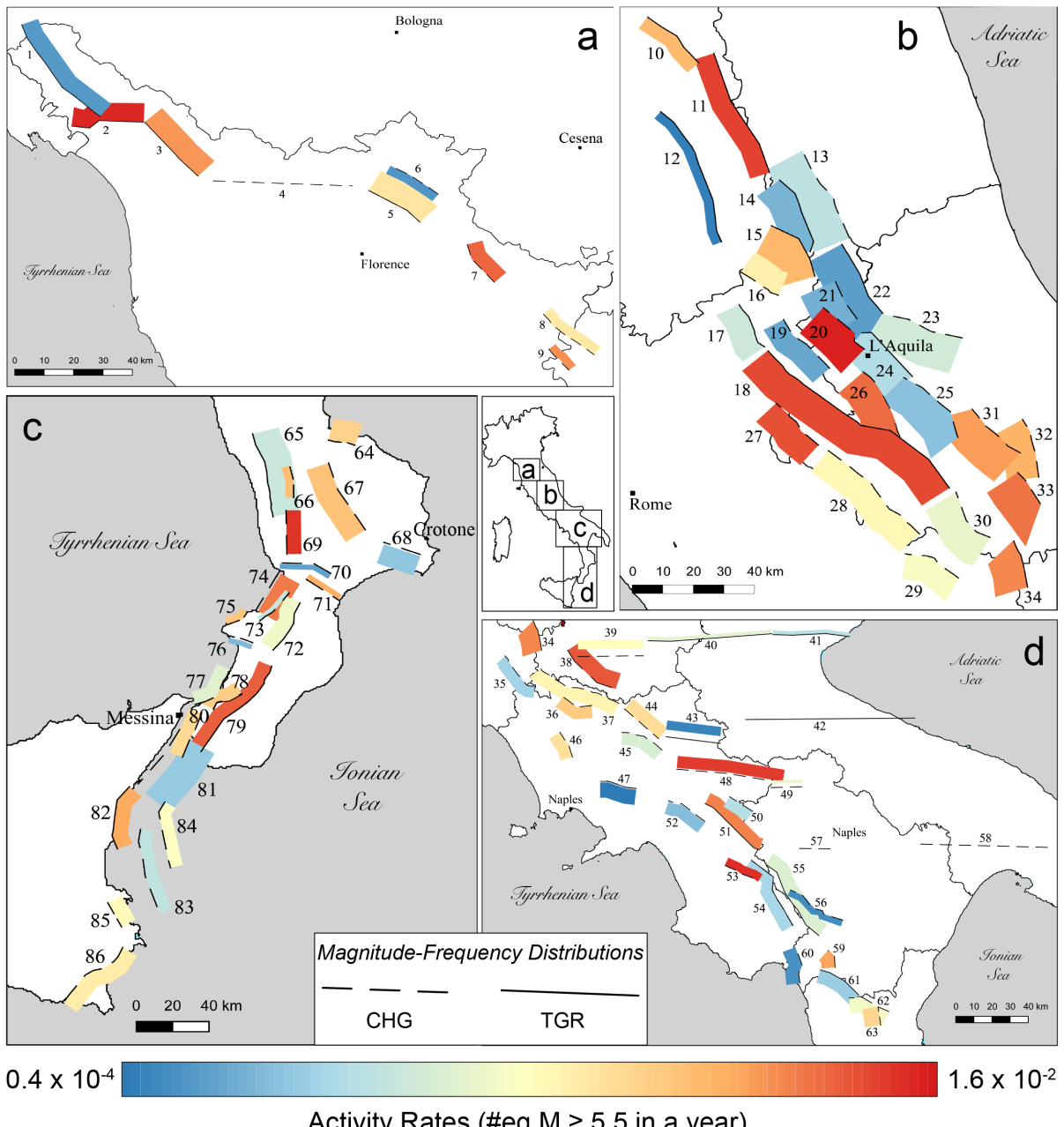
981

982 Fig. 1 a) Map of normal and strike-slip active faults used in this study. The colour  
 983 scale indicates the slip rate. b) Histogram of the slip rate distribution in the entire  
 984 study area and in three subsectors. The numbers 1, 2 and 3 represent the Northern  
 985 Apennines, Central-Southern Apennines and Calabria-Sicilian coast regions,  
 986 respectively. The dotted black lines are the boundaries of the regions.



987

988 Fig. 2 a) Conceptual model of active faults and segmentation rules adopted to define  
 989 a fault source and its planar projection, forming a seismogenic box [modified from  
 990 Boncio et al., 2004]. b) Example of FiSH code output (see Pace et al., 2016 for  
 991 details) for the Paganica fault source showing the magnitude estimates from  
 992 empirical relationships and observations, both of which are affected by uncertainties.  
 993 In this example, four magnitudes are estimated: MMo (blue line) is from the standard  
 994 formula (IASPEI, 2005); MRLD (red line) and MRA (cyan line) correspond to  
 995 estimates based on the maximum subsurface fault length and maximum rupture area  
 996 from the empirical relationships of Wells and Coppersmith (1994) for length and  
 997 area, respectively; and Mobs (magenta line) is the largest observed moment  
 998 magnitude. The black dashed line represents the summed probability density curve  
 999 (SumD), the vertical black line represents the central value of the Gaussian fit of the  
 1000 summed probability density curve (Mmax), and the horizontal black dashed line  
 1001 represents its standard deviation ( $\sigma Mmax$ ). The input values that were used to obtain  
 1002 this output are provided in Table 1. c) Comparison of the magnitude–frequency  
 1003 distributions of the Paganica source, which were obtained using the CHG model (red  
 1004 line) and the TGR model (black line).



1005  
1006 Fig. 3 Maps showing the fault source inputs as seismogenic boxes (see Fig. 2a). The  
1007 colour scale indicates the activity rate. Solid and dashed lines (corresponding to the  
1008 uppermost edge of the fault) are used to highlight our choice between the two end-  
1009 members of the MFD model adopted in the so-called *Mixed* model.

1010  
1011  
1012  
1013  
1014

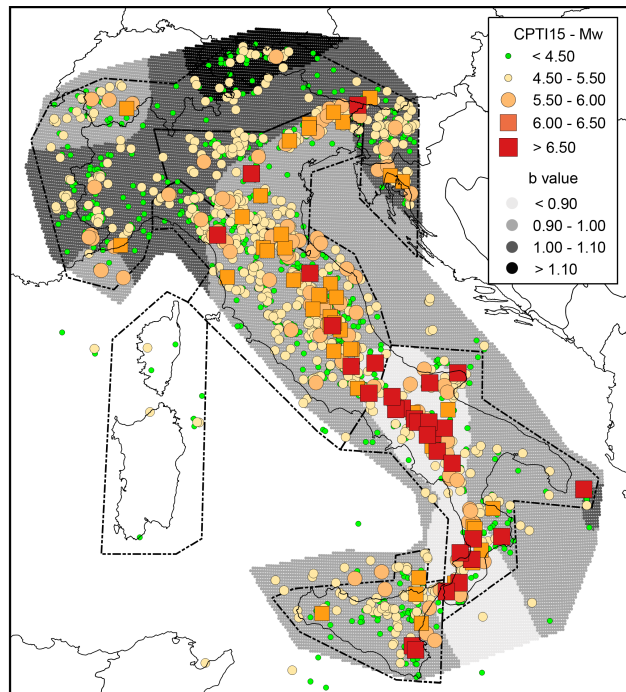


Fig. 4 Historical earthquakes from the most recent version of the historical parametric Italian catalogue (CPTI15, Rovida et al., 2016), the spatial variations in b-values and the polygons defining the five macroseismic areas used to assess the magnitude intervals.



1015  
1016  
1017  
1018

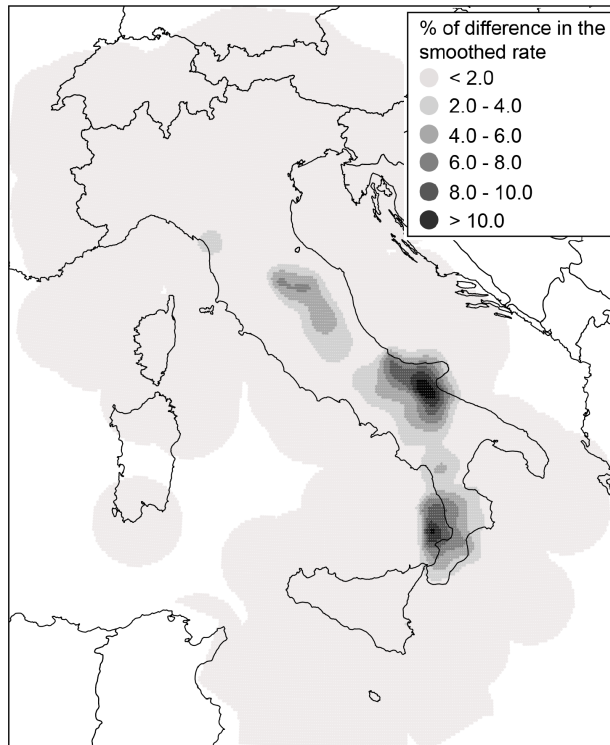
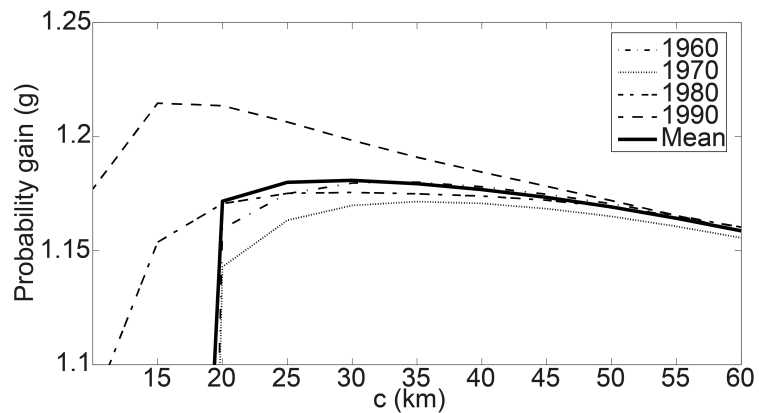
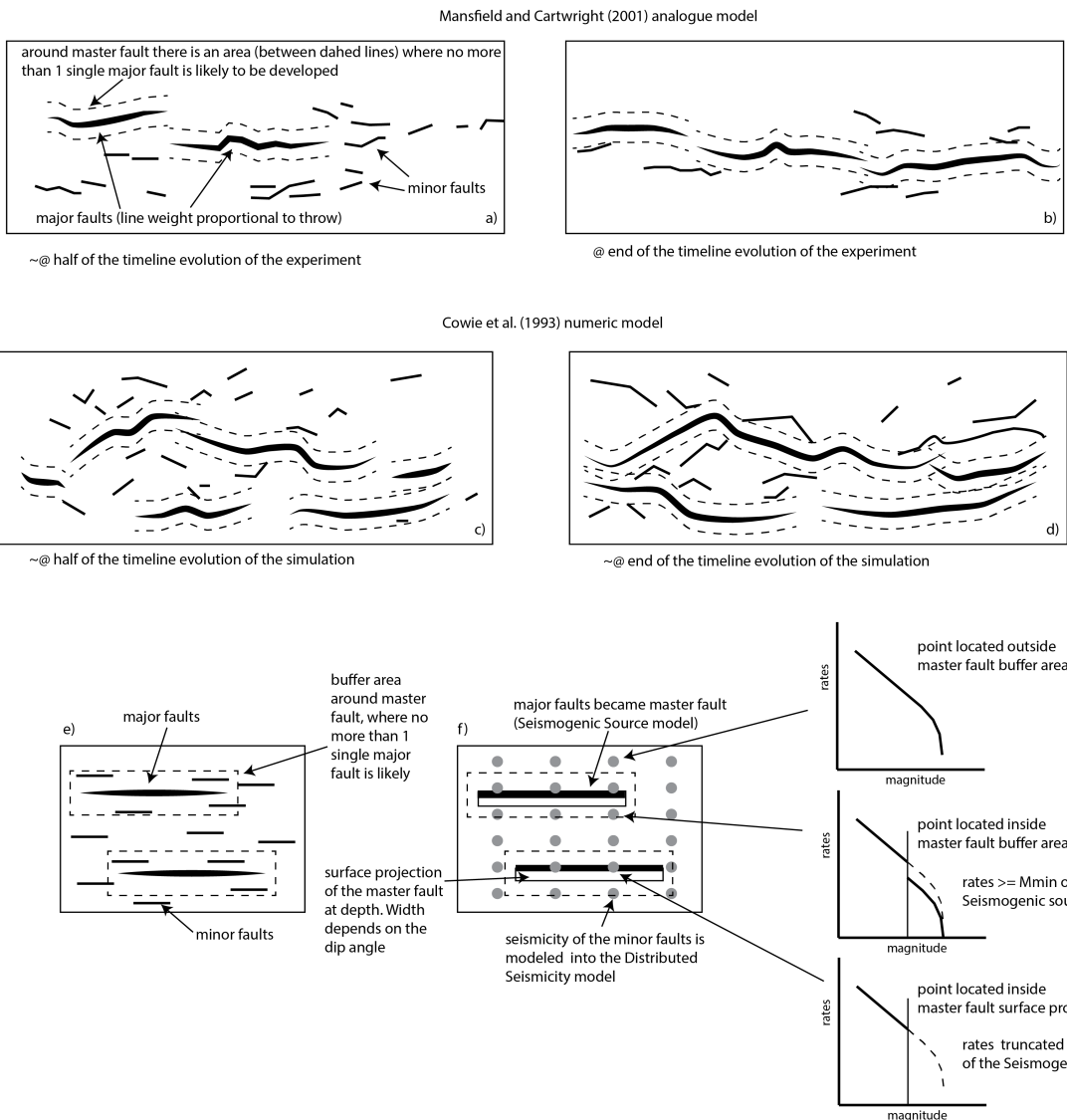


Fig. 5 Differences in percentages between the two smoothed rates produced by eq. (2) using the complete catalogue and the modified catalogue without events associated with known active faults (TGR model)

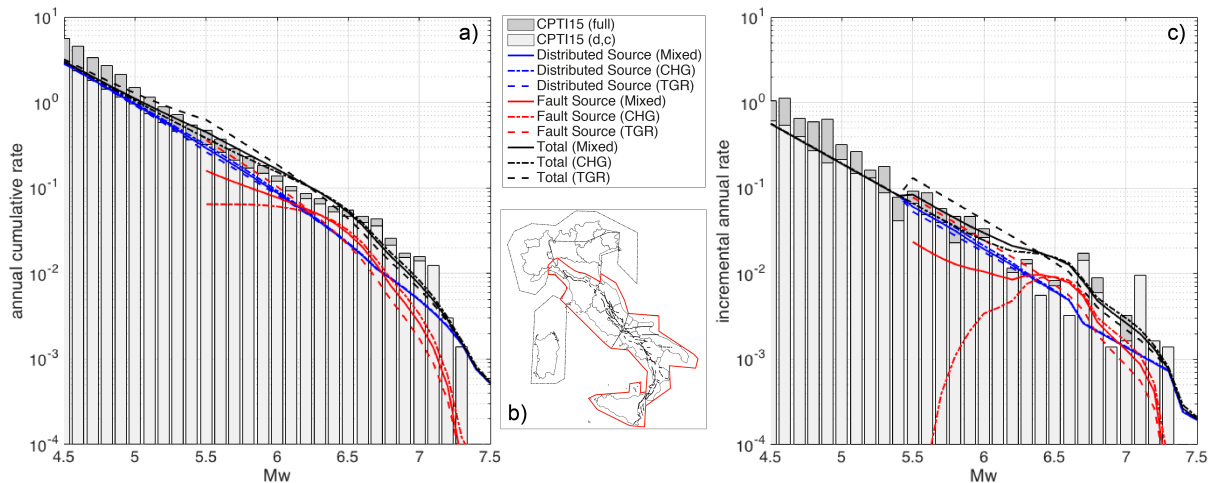


1019  
 1020 Fig. 6 Probability gain per earthquake (see eq. 3) versus correlation distance  $c$ ,  
 1021 ~~highlighting~~ the best radius for use in the smoothed seismicity approach (eq. 2)  
 1022  
 1023  
 1024  
 1025



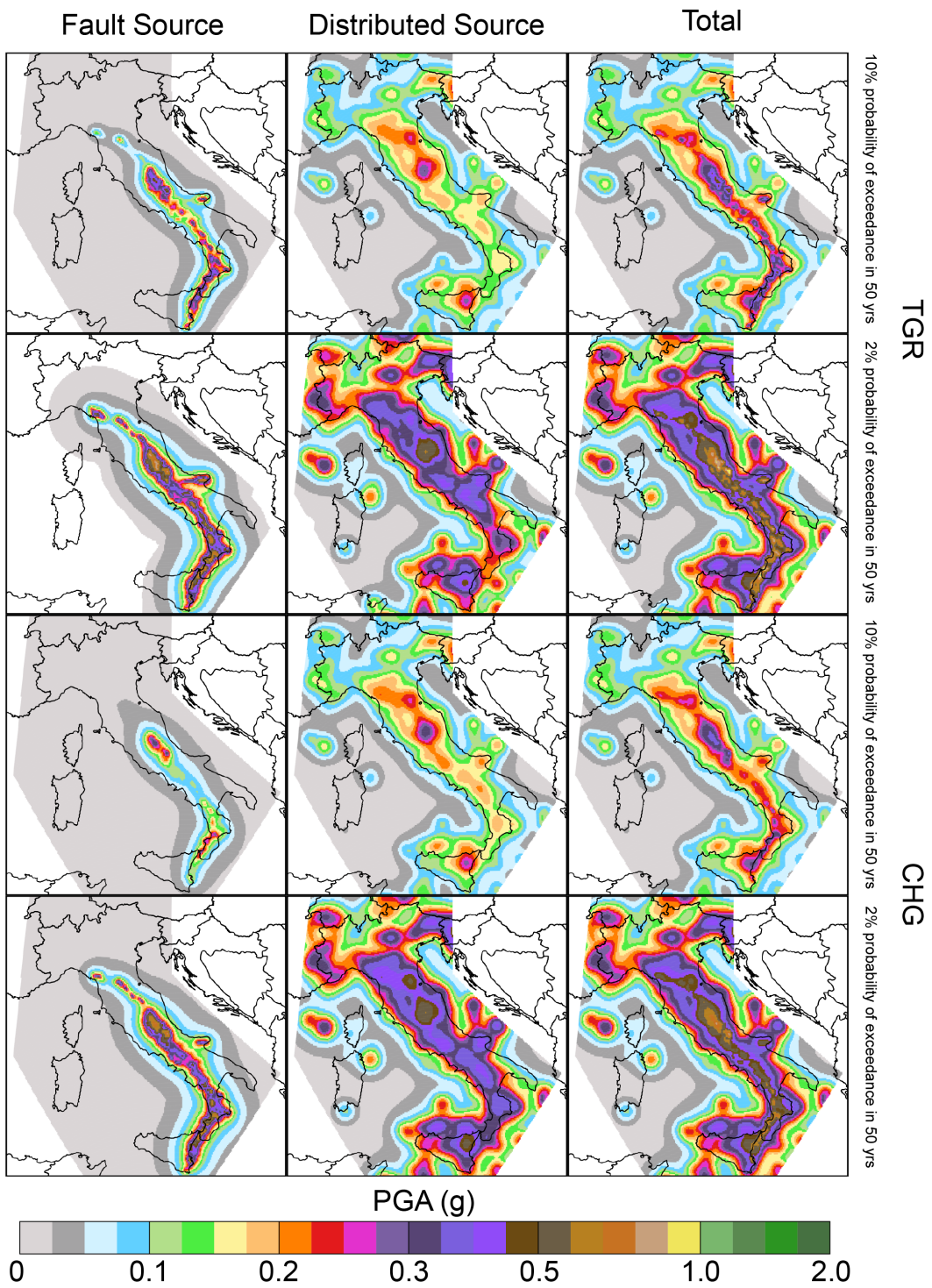
1026

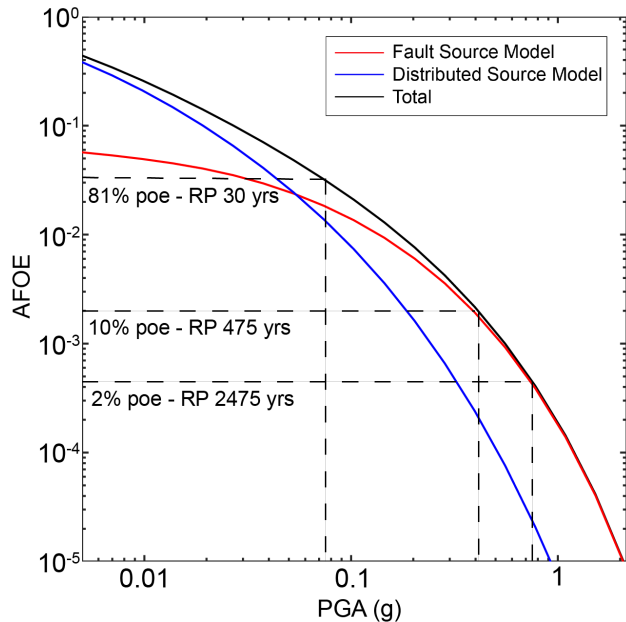
1027 Fig. 7 Fault system evolution and implications in our model. a) and b) Diagrams from  
 1028 the Mansfield and Cartwright (2001) analogue experiment in two different stages: the  
 1029 approximate midpoint of the sequence and the end of the sequence. Areas exist  
 1030 around master faults where no more than a single major fault is likely to develop. c)  
 1031 and d) Diagrams from numerical modelling conducted by Cowie et al. (1993) in two  
 1032 different stages. This experiment shows the similar evolutional features of major and  
 1033 minor faults. e) and f) Application of the analogue and numerical modelling of fault  
 1034 system evolution to the fault source input proposed in this paper. A buffer area is  
 1035 drawn around each fault source, where it is unlikely for other major faults to develop,  
 1036 and it accounts for the length and slip rate of the fault source. This buffer area is  
 1037 useful for reducing or truncating the rates of expected distributed seismicity based on  
 1038 the position of a distributed seismicity point with respect to the buffer zone (see the  
 1039 text for details).



1040 Fig. 8 a) annual cumulative rate and c) incremental annual rate computed for the red  
 1041 bounded area in b). The rates have been computed using: (i) the full CPTI15  
 1042 catalogue; (ii) the declustered and complete catalogue (CPTI15 (d, c) in the legend)  
 1043 obtained using the completeness magnitude thresholds over different periods of time  
 1044 given by Stucchi et al. (2011) for five large zones; (iii) the distributed sources; (iv) the  
 1045 fault sources; and (v) summing fault and distributed sources (Total).  
 1046

1047

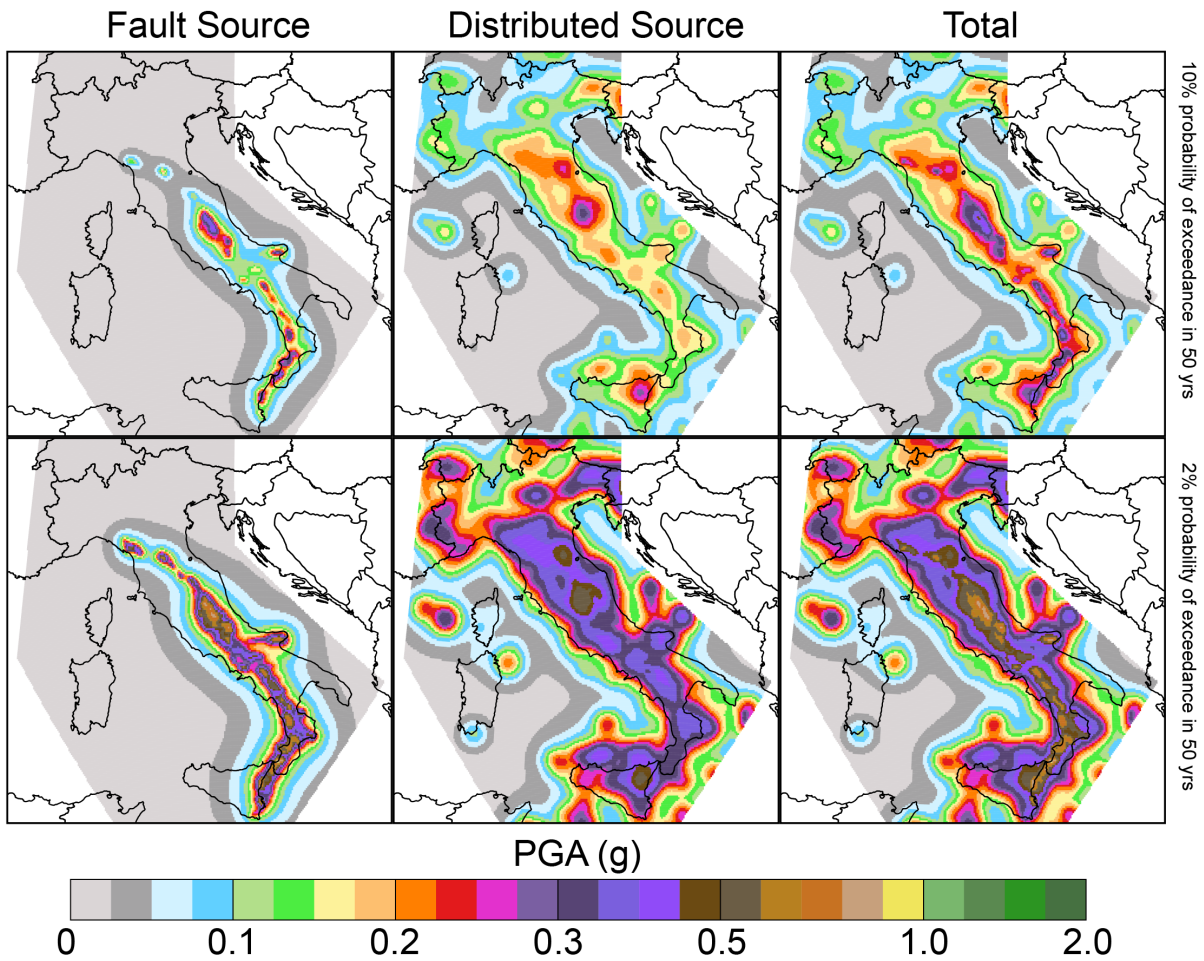




1056

1057 Fig. 10 An example of the contribution to the total seismic hazard level (black line), in  
 1058 terms of hazard curves, by the *fault* (red line) and *distributed* (blue line) source inputs  
 1059 for one of the 45,602 grid points (L'Aquila, 42.400-13.400). The dashed lines  
 1060 represent the 2%, 10% and 81% probabilities of exceedance (poes) in 50 years.

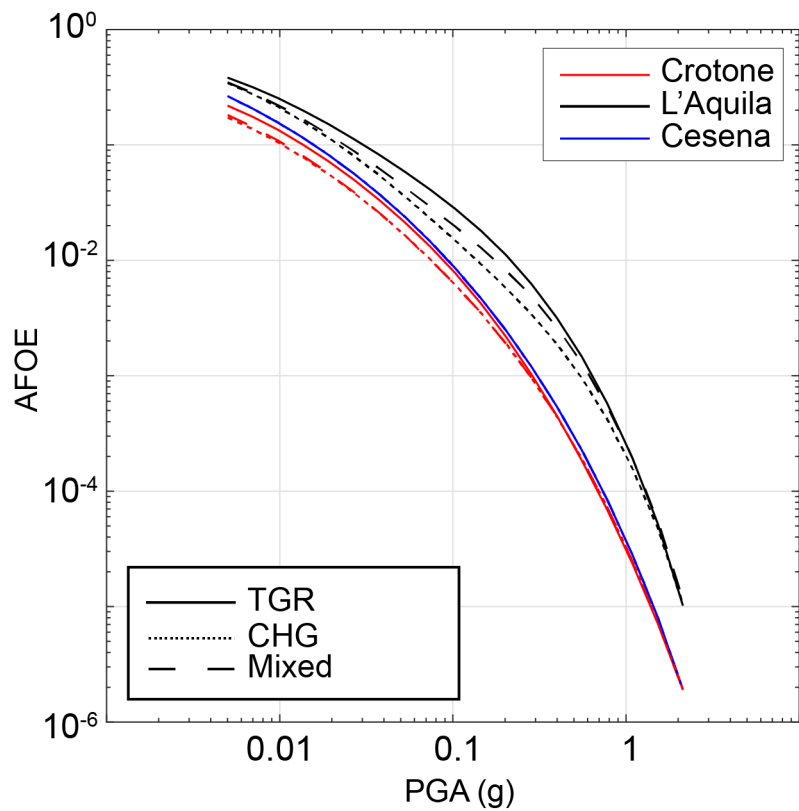
1061



1062

1063

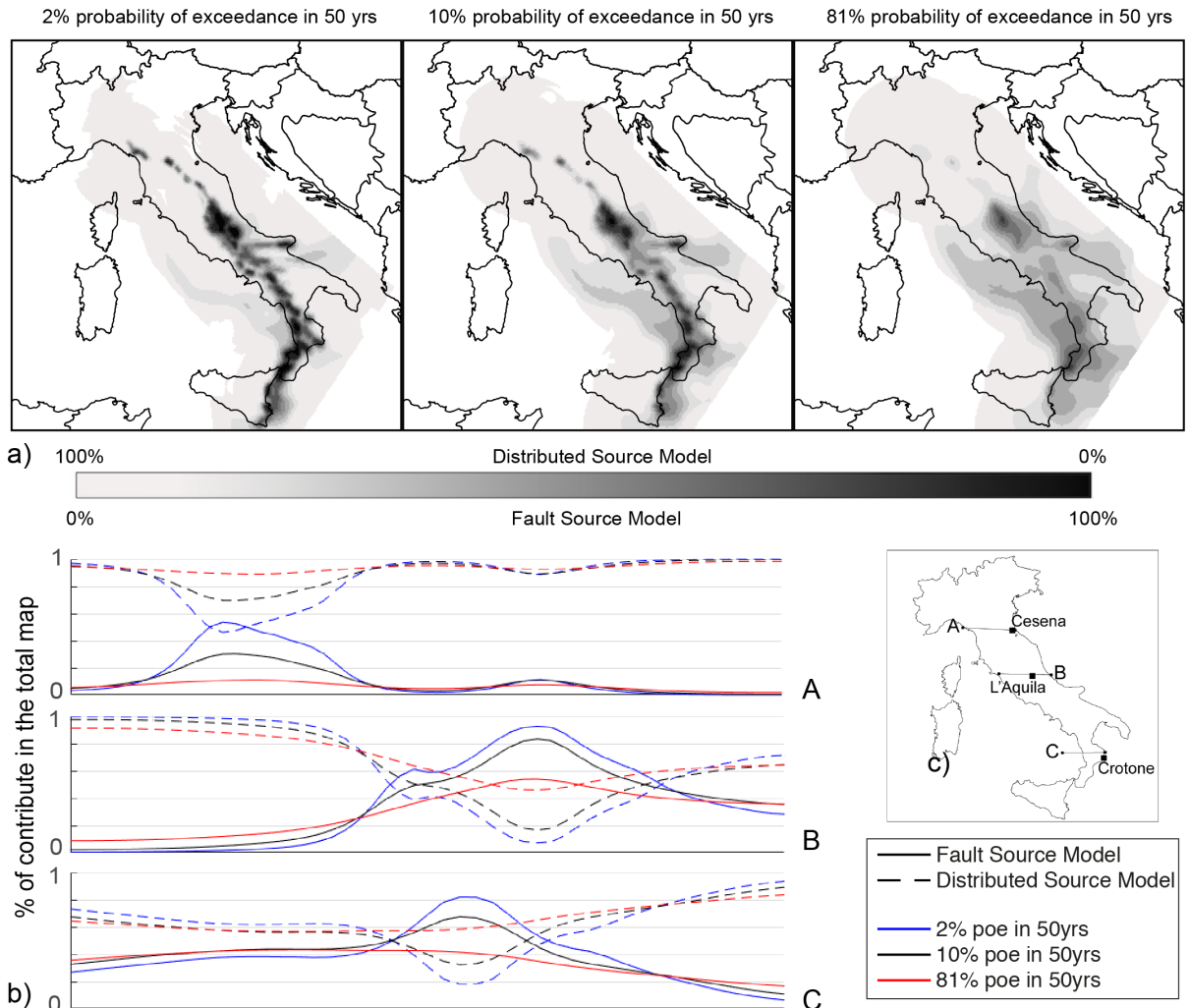
1064 Fig. 11 Seismic hazard maps for the *Mixed* model. The first row shows the fault  
 1065 source, distributed source and total maps computed for 10% probability of  
 1066 exceedance in 50 years, and the second row shows the same maps but computed  
 1067 for 2% probability of exceedance in 50 years, corresponding to return periods of 475  
 1068 and 2475 years, respectively. The results are expressed in terms of peak ground  
 1069 acceleration (PGA).

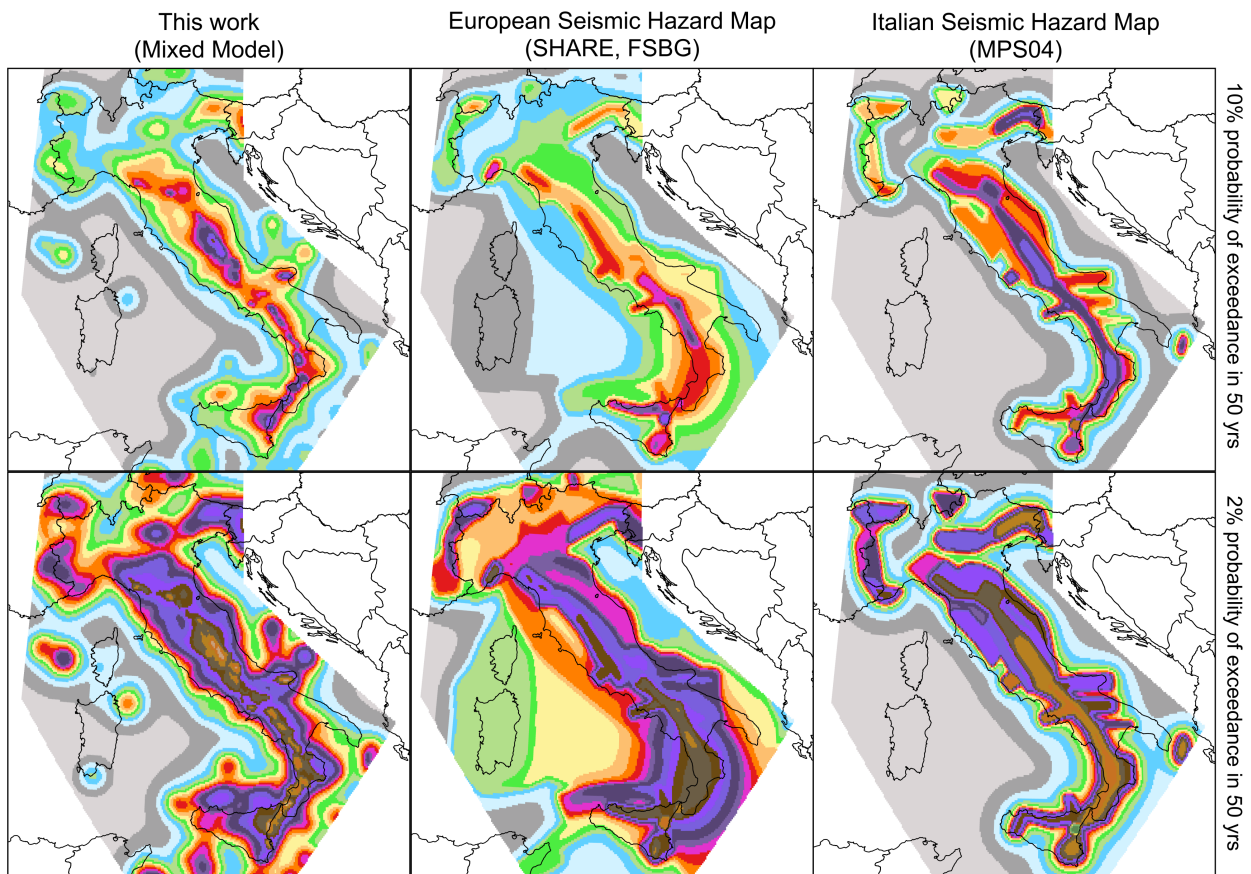


1070  
1071  
1072  
1073

Fig. 12 *CHG* (dotted line), *TGR* (solid line) and *Mixed* model (dashed line) hazard  
curves for three sites: Cesena (red line), L'Aquila (black line) and Crotone (blue line)







1082

1083 Fig. 14 Seismic hazard maps expressed in terms of Peak Ground Acceleration  
 1084 (PGA) and computed for a latitude/longitude grid spacing of  $0.05^\circ$  based on site  
 1085 conditions. The figure shows a comparison of our model (*Mixed model*, on the left),  
 1086 the SHARE model (FSBG logic tree branch, in the middle) and the current Italian  
 1087 national seismic hazard map (MPS04, on the right). The ~~same GMPEs~~ (Akkar et al.  
 1088 2013, Chiou et al., 2008, Faccioli et al., 2010 and Zhao et al., 2006 and Bindi et al.  
 1089 2014), were used for all models to obtain and compare the maps.

1090

1091

1092

1093

1094

1095



ID	Fault Sources	L (km)	Dip (°)	Upper (km)	Lower (km)	SR <sub>min</sub> (mm/yr)	SR <sub>max</sub> (mm/yr)
1	Lunigiana	43.8	40	0	5	0.28	0.7
2	North Apuane Transfer	25.5	45	0	7	0.33	0.83
3	Garfagnana	26.9	30	0	4.5	0.35	0.57
4	Garfagnana Transfer	47.1	90	2	7	0.33	0.83
5	Mugello	21.0	40	0	7	0.33	0.83
6	Ronta	19.3	65	0	7	0.17	0.5
7	Poppi	17.1	40	0	4.5	0.33	0.83
8	Città di Castello	22.9	40	0	3	0.25	1.2
9	M.S.M. Tiberina	10.5	40	0	2.5	0.25	0.75
10	Gubbio	23.6	50	0	6	0.4	1.2
11	Colfiorito System	45.9	50	0	8	0.25	0.9
12	Umbra Valley	51.1	55	0	4.5	0.4	1.2
13	Vettore-Bove	35.4	50	0	15	0.2	1.05
14	Nottoria-Preci	29.0	50	0	12	0.2	1
15	Cascia-Cittareale	24.3	50	0	13.5	0.2	1
16	Leonessa	14.9	55	0	12	0.1	0.7
17	Rieti	17.6	50	0	10	0.25	0.6
18	Fucino	82.3	50	0	13	0.3	1.6
19	Sella di Corno	23.1	60	0	13	0.35	0.7
20	Pizzoli-Pettino	21.3	50	0	14	0.3	1
21	Montereale	15.1	50	0	14	0.25	0.9
22	Gorzano	28.1	50	0	15	0.2	1
23	Gran Sasso	28.4	50	0	15	0.35	1.2
24	Paganica	23.7	50	0	14	0.4	0.9
25	Middle Aternum Valley	29.1	50	0	14	0.15	0.45
26	Campo Felice-Ovindoli	26.2	50	0	13	0.2	1.6
27	Carsoli	20.5	50	0	11	0.35	0.6
28	Liri	42.5	50	0	11	0.3	1.26
29	Sora	20.4	50	0	11	0.15	0.45
30	Marsicano	20.0	50	0	13	0.25	1.2
31	Sulmona	22.6	50	0	15	0.6	1.35
32	Maiella	21.4	55	0	15	0.7	1.6
33	Aremogna C.Miglia	13.1	50	0	15	0.1	0.6
34	Barrea	17.1	55	0	13	0.2	1
35	Cassino	24.6	60	0	11	0.25	0.5
36	Ailano-Piedimonte	17.6	60	0	12	0.15	0.35
37	Matese	48.3	60	0	13	0.2	1.9
38	Bojano	35.5	55	0	13	0.2	0.9
39	Frosolone	36.1	70	11	25	0.35	0.93
40	Ripabottoni-San Severo	68.3	85	6	25	0.1	0.5
41	Mattinata	42.3	85	0	25	0.7	1
42	Castelluccio dei Sauri	93.2	90	11	22	0.1	0.5
43	Ariano Irpino	30.1	70	11	25	0.35	0.93
44	Tammaro	25.0	60	0	13	0.35	0.93
45	Benevento	25.0	55	0	10	0.35	0.93
46	Volturno	15.7	60	1	13	0.23	0.57
47	Avella	20.5	55	1	13	0.2	0.7
48	Ufita-Bisaccia	59.0	64	1.5	15	0.35	0.93
49	Melfi	17.2	80	12	22	0.1	0.5
50	Irpinia Antithetic	15.0	60	0	11	0.2	0.53

51	Irpinia	39.7	65	0	14	0.3	2.5
52	Volturara	23.7	60	1	13	0.2	0.35
53	Alburni	20.4	60	0	8	0.35	0.7
54	Caggiano-Diano Valley	46.0	60	0	12	0.35	1.15
55	Pergola-Maddalena	50.6	60	0	12	0.20	0.93
56	Agri	34.9	50	5	15	0.8	1.3
57	Potenza	17.8	90	15	21	0.1	0.5
58	Palagianello	73.3	90	13	22	0.1	0.5
59	Monte Alpi	10.9	60	0	13	0.35	0.9
60	Maratea	21.6	60	0	13	0.46	0.7
61	Mercure	25.8	60	0	13	0.2	0.6
62	Pollino	23.8	60	0	15	0.22	0.58
63	Castrovilliari	10.3	60	0	15	0.2	1.15
64	Rossano	14.9	60	0	22	0.5	0.6
65	Crati West	49.7	45	0	15	0.84	1.4
66	Crati East	18.4	60	0	8	0.75	1.45
67	Lakes	43.6	60	0	22	0.75	1.45
68	Fuscalto	21.1	60	2	22	0.75	1.45
69	Piano Lago-Decollatura	25.0	60	1	15	0.23	0.57
70	Catanzaro North	29.5	80	3	20	0.75	1.45
71	Catanzaro South	21.3	80	3	20	0.75	1.45
72	Serre	31.6	60	0	15	0.7	1.15
73	Vibo	23.0	80	0	15	0.75	1.45
74	Sant'Eufemia Gulf	24.8	40	1	11	0.11	0.3
75	Capo Vaticano	13.7	60	0	8	0.75	1.45
76	Coccorino	13.3	70	3	11	0.75	1.45
77	Scilla	29.7	60	0	13	0.8	1.5
78	Sant'Eufemia	19.2	60	0	13	0.75	1.45
79	Cittanova-Armo	63.8	60	0	13	0.45	1.45
80	Reggio Calabria	27.2	60	0	13	0.7	2
81	Taormina	38.7	30	3	13	0.9	2.6
82	Acireale	39.4	60	0	15	1.15	2.3
83	Western Ionian	50.1	65	0	15	0.75	1.45
84	Eastern Ionian	39.3	65	0	15	0.75	1.45
85	Climiti	15.7	60	0	15	0.75	1.45
86	Avola	46.9	60	0	16	0.8	1.6

1096

1097 Table 1 Geometric Parameters of the Fault Sources. L, along-strike length; Dip,  
 1098 inclination angle of the fault plane; Upper and Lower, the thickness bounds of the  
 1099 local seismogenic layer; SRmin and SRmax, the slip rates assigned to the sources  
 1100 using the references available (see the supplemental files); and ID, the fault number  
 1101 identifier.

1102

ID	Fault Sources	Historical Earthquakes				Instrumental Earthquakes		
		yyyy/mm/dd	$I_{Max}$	$I_0$	$M_w$	$sD$	yyyy/mm/dd	$M_w$
1	Lunigiana	1481/05/07	VIII	VIII	5.6	0.4		
		1834/02/14	IX	IX	6.0	0.1		
2	North Apuane Transfer	1837/04/11	X	IX	5.9	0.1		
3		1740/03/06	VIII	VIII	5.6	0.2		
4	Garfagnana Transfer	1920/09/07	X	X	6.5	0.1		
5		Mugello	1542/06/13	IX	IX	6.0	0.2	
			1919/06/29	X	X	6.4	0.1	
6	Ronta							
7								
8	Città di Castello	1269			5.7			
		1389/10/18	IX	IX	6	0.5		
		1458/04/26	VIII-IX	VIII-IX	5.8	0.5		
		1789/09/30	IX	IX	5.9	0.1		
9		M.S.M. Tiberina	1352/12/25	IX	IX	6.3	0.2	
		1917/04/26	IX-X	IX-X	6.0	0.1		
10	Gubbio						1984/04/29	5.6
11		Colfiorito System	1279/04/30	X	IX	6.2	0.2	1997/09/26
			1747/04/17	IX	IX	6.1	0.1	1997/09/26
			1751/07/27	X	X	6.4	0.1	6
12	Umbra Valley	1277		VIII	5.6	0.5		
		1832/01/13	X	X	6.4	0.1		
		1854/02/12	VIII	VIII	5.6	0.3		
13	Vettore-Bove						2016/10/30	6.5
14		Nottoria-Preci	1328/12/01	X	X	6.5	0.3	1979/09/19
			1703/01/14	XI	XI	6.9	0.1	
			1719/06/27	VIII	VIII	5.6	0.3	
			1730/05/12	IX	IX	6.0	0.1	
			1859/08/22	VIII-IX	VIII-IX	5.7	0.3	
			1879/02/23	VIII	VIII	5.6	0.3	
15	Cascia-Cittareale	1599/11/06	IX	IX	6.1	0.2		
		1916/11/16	VIII	VIII	5.5	0.1		
16	Leonessa							
17		Rieti	1298/12/01	X	IX-X	6.3	0.5	
			1785/10/09	VIII-IX	VIII-IX	5.8	0.2	
18	Fucino	1349/09/09	IX	IX	6.3	0.1		
		1904/02/24	IX	VIII-IX	5.7	0.1		
		1915/01/13	XI	XI	7	0.1		
19	Sella di Corno							
20		Pizzoli-Pettino	1703/02/02	X	X	6.7	0.1	
21								
22	Montereale	Gorzano	1639/10/07	X	IX-X	6.2	0.2	
			1646/04/28	IX	IX	5.9	0.4	
23	Gran Sasso							
24		Paganica	1315/12/03	VIII	VIII	5.6	0.5	2009/06/04
			1461/11/27	X	X	6.5	0.5	6.3
25	Middle Aternum Valley							
26		Campo Felice-Ovindoli						
27								
28		Carsoli						
29								
30	Liri							
31		Sora						
32								
33	Marsicano							
34		Sulmona						
35								
36	Maiella							
37		Aremogna C.Miglia						
							1984/05/07	5.9
		Barrea						
		Cassino						
		Ailano-Piedimonte						
		Matese						
			1349/09/09	X-XI	X	6.8	0.2	

38	Bojano	1805/07/26	X	X	6.7	0.1		
39	Frosolone	1456/12/05	XI	XI	7	0.1		
40	Ripabottoni-San Severo	1627/07/30	X	X	6.7	0.1	2002/10/31	5.7
		1647/05/05	VII-VIII	VII-VIII	5.7	0.4		
		1657/01/29	IX-X	VIII-IX	6.0	0.2		
41	Mattinata	1875/12/06	VIII	VIII	5.9	0.1		
		1889/12/08	VII	VII	5.5	0.1		
		1948/08/18	VII-VIII	VII-VIII	5.6	0.1		
42	Castelluccio dei Sauri	1361/07/17	X	IX	6	0.5		
		1560/05/11	VIII	VIII	5.7	0.5		
		1731/03/20	IX	IX	6.3	0.1		
43	Ariano Irpino	1456/12/05			6.9	0.1		
		1962/08/21	IX	IX	6.2	0.1		
44	Tammaro	1688/06/05	XI	XI	7	0.1		
45	Benevento							
46	Volturno							
47	Avella	1499/12/05	VIII	VIII	5.6	0.5		
48	Ufita-Bisaccia	1732/11/29	X-XI	X-XI	6.8	0.1		
		1930/07/23	X	X	6.7	0.1		
49	Melfi	1851/08/14	X	X	6.5	0.1		
50	Irpinia Antithetic							
51	Irpinia	1466/01/15	VIII-IX	VIII-IX	6.0	0.2	1980/11/23	6.8
		1692/03/04	VIII	VIII	5.9	0.4		
		1694/09/08	X	X	6.7	0.1		
		1853/04/09	IX	VIII	5.6	0.2		
52	Volturara							
53	Alburni							
54	Caggiano-Diano Valley	1561/07/31	IX-X	X	6.3	0.1		
55	Pergola-Maddalena	1857/12/16			6.5			
		1857/12/16			6.3			
56	Agri							
57	Potenza	1273/12/18	VIII-IX	VIII-IX	5.8	0.5	1990/05/05	5.8
58	Palagianello							
59	Monte Alpi							
60	Maratea							
61	Mercure	1708/01/26	VIII-IX	VIII	5.6	0.6	1998/09/09	5.5
62	Pollino							
63	Castrovilli							
64	Rossano	1836/04/25	X	IX	6.2	0.2		

65	Crati West	1184/05/24 1870/10/04 1886/03/06	IX X VII-VIII	IX IX-X VII-VIII	6.8 6.2 5.6	0.3 0.1 0.3
66	Crati East	1767/07/14 1835/10/12	VIII-IX X	VIII-IX IX	5.9 5.9	0.2 0.3
67	Lakes	1638/06/08	X	X	6.8	0.1
68	Fuscalto	1832/03/08	X	X	6.6	0.1
69	Piano Lago-Decollatura					
70	Catanzaro North	1638/03/27			6.6	
71	Catanzaro South	1626/04/04	X	IX	6.1	0.4
72	Serre	1659/11/05 1743/12/07 1783/02/07 1791/10/13	X IX-X X-XI IX	X VIII-IX X-XI IX	6.6 5.9 6.7 6.1	0.1 0.2 0.1 0.1
73	Vibo					
74	Sant'Eufemia Gulf	1905/09/08	X-XI	X-XI	7	0.1
75	Capo Vaticano					
76	Coccorino	1928/03/07	VIII	VII-VIII	5.9	0.1
77	Scilla					
78	Sant'Eufemia	1894/11/16	IX	IX	6.1	0.1
79	Cittanova-Armo	1509/02/25 1783/02/05	IX XI	VIII XI	5.6 7.1	0.4 0.1
80	Reggio Calabria					
81	Taormina	1908/12/28	XI	XI	7.1	0.2
82	Acireale	1818/02/20	IX-X	IX-X	6.3	0.1
83	Western Ionian	1693/01/11	XI	XI	7.3	0.1
84	Eastern Ionian					
85	Climiti					
86	Avola					

1103

1104 Table 2 Earthquake-Source Association Adopted for Fault Sources.  $I_{Max}$ , maximum  
 1105 intensity;  $I_0$ , epicentral intensity;  $M_w$ , moment magnitude; and  $sD$ , standard deviation  
 1106 of the moment magnitude. For references, see the supplemental files.